

# MOLECULAR GAS DYNAMICS OF THE STRONGLY-LENSED WET-MERGER RXS J1131–1231 AT $Z=0.654$

T. K. DAISY LEUNG, DOMINIK A. RIECHERS, AND RICCARDO PAVESI

Department of Astronomy, Space Sciences Building, Cornell University, Ithaca, NY 14853, USA; tleung@astro.cornell.edu

*To be submitted to the ApJ*

## ABSTRACT

We report observations of the CO( $J=2 \rightarrow 1$ ) and CO( $J=3 \rightarrow 2$ ) line emission towards the quadruply-imaged quasar RXS J1131–1231 at  $z=0.654$  obtained using the Plateau de Bure Interferometer (PdBI) and Combined Array for Research in Millimeter-wave Astronomy (CARMA), making this the first spatially resolved CO study at intermediate redshift. Our lens modeling shows that the highly asymmetric double-horned line profile observed in the CO( $J=2 \rightarrow 1$ ) spectrum is mainly a result of differential lensing, where the magnification factor varies from  $\sim 3$  to  $\sim 8$  across different kinematic components. The intrinsically symmetric line profile with a clear velocity gradient in the source-plane suggests that the quasar host galaxy is a rotating disk. In addition, we find a secondary CO-emitting source near RXJ1131 whose location is consistent with the optically-faint companion reported in previous studies. The lensing-corrected gas mass of  $M_{\text{gas}} \sim 1.4 \times 10^{10} M_{\odot}$  inferred for RXJ1131 and  $\sim 2 \times 10^9 M_{\odot}$  for its companion correspond to a gas mass ratio of  $\sim 7:1$ . The extended CO gas disk in RXJ1131 ( $R \sim 6$  kpc) yields a dynamical mass of  $M_{\text{dyn}} \sim 8 \times 10^{10} M_{\odot}$ , and thus a gas mass fraction of  $\sim 19\%$ , which is consistent with the trend of decreasing molecular gas fraction since  $z \sim 1$ . The lensing-corrected  $M^* \sim 3 \times 10^{10} M_{\odot}$ ,  $M_{\text{dust}} \sim 4 \times 10^8 M_{\odot}$ ,  $L_{\text{IR}} \sim 1.5 \times 10^{12} L_{\odot}$ , and  $\text{SFR}_{\text{FIR}} = 120 \pm 63 M_{\odot} \text{ yr}^{-1}$  of RXJ1131 together with the source-plane morphology of the gas and the stellar populations suggest that ongoing starbursts are embedded within the molecular gas reservoir, and that the nuclear starbursts are likely triggered by interactions with the companion. The  $M_{\text{BH}}/M_{\text{bulge}}$  of  $\gtrsim 0.27\%$  derived for RXJ1131 lies above the local relation but is consistent with other radio-loud galaxies at this epoch, suggesting that the co-evolution between RXJ1131 and its host galaxy is different than those of local AGN host galaxies.

*Subject headings:* ISM: molecules – infrared: galaxies – galaxies: mergers – galaxies: starburst – galaxies: evolution – quasars: individual (RXS J1131–1231)

## 1. INTRODUCTION

Studies of galaxy evolution have been focusing on the interplay between star formation and active galactic nucleus (AGN) activity across cosmic epochs. It is not well-understood when and how stellar populations of present-day galaxies were assembled, but it is clear that both the co-moving star formation rate and black hole accretion rate densities increased substantially since  $z > 3$  and reached their climax at  $z \sim 2$ , followed by a rapid decline toward  $z \sim 0$  (e.g., Hopkins & Beacom 2006; Madau & Dickinson 2014). A leading explanation for this decline is related to the evolution of molecular gas content and star formation efficiency (Erb et al. 2006; Carilli & Walter 2013; Walter et al. 2014), but confirmation from direct molecular gas measurements at intermediate redshift ( $0.2 < z < 1$ ) is still limited both in number and in the variety of galaxy populations probed — only unresolved CO observations have been carried out for  $\sim 70$  ULIRGs up to date (Combes et al. 2011, 2013).

Meanwhile, empirical scaling relations such as the  $M_{\text{BH}}-M_{\text{bulge}}$  relation (e.g., Magorrian et al. 1998; Häring & Rix 2004) has been established locally, suggesting a co-eval growth between local SMBHs and their host galaxies. Attempts to extend this relation out to higher redshifts, beyond the peak epoch of star formation and AGN activity, have been made in recent years. It has been reported

that the  $M_{\text{BH}}/M_{\text{bulge}}$  ratio of high- $z$  submillimeter galaxies (SMGs) falls below the local relation (e.g., Borys et al. 2005; Alexander et al. 2008) but that of high- $z$  quasar host galaxies is found lying above the relation (e.g., McLure et al. 2006; Peng et al. 2006). Stellar mass of quasar host galaxies at  $z > 4$  constrained by their CO-based dynamical mass is also too small compared to that based on the local relation (Walter et al. 2004; Riechers et al. 2008; Coppin et al. 2008). While it has become clearer that high- $z$  galaxies deviate from the local relation, and among their galaxy populations, such a picture is still unclear at intermediate redshift. This is owed to the difficulties in measuring stellar emission in the host galaxy under the presence of a bright quasar, or alternatively due to the lack of spatially resolved CO observations to provide dynamical constraints on the stellar mass. With gravitational lensing, emission of the background quasar and its host galaxy is magnified and stretched out to different extents, and is being projected onto different locations in the image plane, allowing spatially resolved measurements their emission in a relatively uncontaminated fashion.

The quasar RXS J113151.62–123158 (hereafter RXJ1131) at  $z_{\text{s, QSO}}=0.685$  (Sluse et al. 2003, hereafter S03) is a particularly well-suited source for studying the evolution of molecular gas properties in quasar host galaxies and the connection between SMBHs and their host galaxies at intermediate redshift given its unique

lensing configuration. The stellar emission in the host galaxy of RXJ1131 is lensed into an Einstein ring of radius  $1''.83$  that is clearly separated from the quadruply imaged quasar emission (Claeskens et al. 2006, hereafter C06). We have thus carried out a detailed study of RXJ1131 as presented in this paper. RXJ1131 is strongly lensed by an elliptical galaxy at  $z_L = 0.295$  (S03). The moderate mass black hole  $M_{\text{BH}} = 8 \times 10^7 M_\odot$  (Sluse et al. 2012) residing in RXJ1131 is rotating with a high spin parameter ( $a \sim 0.9$ ; Reis et al. 2014), and is radiating at an intrinsic bolometric luminosity of  $L_{\text{bol,X}} = 1.3 \times 10^{45} \text{ erg s}^{-1}$  (Pooley et al. 2007).

This paper is structured as follows. In §2, we outline details of the observations and of our data reduction procedures. In §3, we describe the astrometric corrections applied to align an *HST* image with an VLA radio image. In §4, we report measurements of the  $\text{CO}(J=2 \rightarrow 1)$  and  $\text{CO}(J=3 \rightarrow 2)$  lines and broadband photometry spanning the optical to radio wavelengths. In §5, we present dynamical lens modeling of the  $\text{CO}(J=2 \rightarrow 1)$  data and SED modeling of the host galaxy of RXJ1131 to derive physical parameters reflecting the nature of this system. In §6, we discuss the merger stage of RXJ1131, the velocity offset between the AGN lines and the CO lines, and the  $M_{\text{BH}}-M_{\text{dyn}}$  relation of RXJ1131. Finally, we summarize the main results and present our conclusions in §7. We use a concordance  $\Lambda$ CDM cosmology throughout this paper, with parameters from the WMAP9 results:  $H_0 = 69.32 \text{ km s}^{-1} \text{ Mpc}^{-1}$ ,  $\Omega_M = 0.29$ , and  $\Omega_\Lambda = 0.71$  (Hinshaw et al. 2013).

## 2. OBSERVATIONS

### 2.1. PdBI CO( $J=2 \rightarrow 1$ )

Observations of the  $\text{CO}(J=2 \rightarrow 1)$  rotational line ( $\nu_{\text{rest}} = 230.538 \text{ GHz}$ ) redshifted to  $\nu_{\text{obs}} \sim 139.0 \text{ GHz}$  were carried out using IRAM Plateau de Bure Interferometer (PdBI; Program ID: S14BX; PI: D. Riechers). Two observing runs were carried out on 2014 December 06 and 2015 February 05 under good weather conditions in the C and D array configurations, respectively. The 2 mm receivers were used to cover the redshifted  $\text{CO}(J=2 \rightarrow 1)$  line and the underlying continuum emission, employing a correlator setup that provides an effective bandwidth of 3.6 GHz (dual polarization) and a spectral resolution of 10.0 MHz ( $\sim 21.5 \text{ km s}^{-1}$ ). This resulted in 3.75 hours of cumulative six antenna-equivalent on-source time after discarding unusable visibility data. The nearby quasars B1127–145 and B1124–186 were observed every 22 minutes for pointing, secondary amplitude, and phase calibration, and B1055+018 was observed as the bandpass calibrator for both tracks. MWC349 and 3C279 were observed as primary flux calibrators for the C and D array observations, respectively, yielding calibration accuracy better than 15%.

The GILDAS package was used to calibrate and analyze the visibility data. The calibrated visibility data were imaged and deconvolved using the CLEAN algorithm with “natural” weighting. This yields a synthesized clean beam size of  $4''.44 \times 1''.95$  (PA =  $13^\circ$ ). The final rms noise is

$\sigma = 1.45 \text{ mJy beam}^{-1}$  over 10 MHz ( $21.5 \text{ km s}^{-1}$ ). The continuum image at  $\nu_{\text{cont}} \sim 139 \text{ GHz}$  is produced by averaging over 3.16 GHz of line-free bandwidth. This yields an rms noise of  $0.082 \text{ mJy beam}^{-1}$ .

### 2.2. CARMA CO( $J=3 \rightarrow 2$ )

Observations of the  $\text{CO}(J=3 \rightarrow 2)$  rotational line in RXJ1131 ( $\nu_{\text{rest}} = 345.7959899 \text{ GHz}$ ) redshifted to  $\nu_{\text{obs}} = 208.6 \text{ GHz}$  were carried out with the Combined Array for Research in Millimeter-wave Astronomy (CARMA; Program ID: cf0098; PI: D. Riechers) in the D array configuration on 2014 February 02 under poor 1.5 mm weather conditions and on 2014 February 17 under good 1.5 mm weather conditions. The correlator setup provides a bandwidth of 3.75 GHz in each sideband and a spectral resolution of 12.5 MHz ( $\sim 17.9 \text{ km s}^{-1}$ ). The line was placed in the lower sideband with the local oscillator tuned to  $\nu_{\text{LO}} \sim 216 \text{ GHz}$ . The radio quasars J1127–189 (first track) and 3C273 (second track) were observed every 15 minutes for pointing, amplitude, and phase calibration. Mars was observed as the primary absolute flux calibrator and 3C279 was observed as the bandpass calibrator for both tracks. This results in a total on-source time of 2.94 hours after flagging poor visibility data.

Given that the phase calibrator used for the first track was faint and was observed under poor weather conditions and that the phase calibrator used for the second track was far from our target source, the phase calibration is sub-par, with an rms scatter  $\sim 50^\circ$  over a baseline length of  $\sim 135 \text{ m}$ . We thus conservatively estimate a calibration accuracy of  $\sim 35\%$  based on the flux scale uncertainties, the gain variations over time, and the phase scatter on the calibrated data. We therefore treat its line intensity with caution and ensure that our physical interpretation of this system and the conclusion of this paper do not rely on this quantity.

The MIRIAD package was used to calibrate the visibility data. The calibrated visibility data were imaged and deconvolved using the CLEAN algorithm with “natural” weighting. This yields a synthesized clean beam size of  $3''.2 \times 1''.9$  (PA =  $8^\circ$ ) for the lower sideband image cube. The final rms noise is  $\sigma = 13.3 \text{ mJy beam}^{-1}$  over a channel width of 25 MHz. An rms noise of  $\sigma = 0.83 \text{ mJy beam}^{-1}$  is reached by averaging over the line-free channels in both sidebands.

### 2.3. VLA (Archival)

Our analysis also uses archival data of the 5 GHz radio continuum obtained with the Very Large Array (VLA; Program ID: AW741; PI: Wucknitz). Observations were carried out on 2008 December 29 under excellent weather conditions in the A array configuration for a total of  $\sim 7$  hours on-source time. The C-band receivers were used with a continuum mode setup, providing a bandwidth of 50 MHz for the two IF bands with full polarization. The nearby radio quasar J1130–149 was observed every 10 minutes for pointing, amplitude, and phase calibration, J1331+305 was observed as the primary flux calibrator, and J0319+415 was observed as the bandpass calibrator,

yielding  $\sim 10\%$  calibration accuracy. We used AIPS to calibrate the visibility data. The calibrated visibility data were imaged and deconvolved using the CLEAN algorithm with robust=0, which was chosen to obtain a higher resolution image given high SNR. This yields a synthesized clean beam size of  $0''.49 \times 0''.35$  (PA= $0.18^\circ$ ) and a final rms noise of  $\sigma = 13 \mu\text{Jy beam}^{-1}$ .

### 3. HST ASTROMETRY

We obtained an *HST* image taken with the ACS/Wide Field Camera using the F555W filter (V-band) from the Hubble Legacy Archive<sup>1</sup>. The details of the observations can be found in C06. We adopt the VLA 5 GHz map as the reference coordinate frame to align the optical (V-band) image. We shift the latter to the east by  $0''.5963$  in R.A. and  $+0''.8372$  in Dec., which is consistent with the typical astrometric precision ( $1''$ – $2''$ ) of images from the Hubble Legacy Archive<sup>2</sup>. This astrometric correction is critical to avoid artificial spatial offsets between different emitting regions and to carry out our lens modeling, in which the absolute position of the foreground lensing galaxy is based on its coordinates in the high-resolution optical image. The VLA image is calibrated using a well-monitored phase calibrator, with absolute positional accuracy of  $\sim 2$  mas. For this reason, the absolute alignment between the VLA image and other interferometric images reported in this paper are expected to have an astrometric precision better than  $0''.1$ , modulo uncertainties related to the SNR and phase instability.

## 4. RESULTS

### 4.1. $\text{CO}(J=2 \rightarrow 1)$ Emission

We detect  $\text{CO}(J=2 \rightarrow 1)$  line emission toward the background source in the PdBI data at  $\gtrsim 27\sigma$  significance, confirming the redshift at  $z_{\text{CO}} = 0.6537 \pm 0.0005$ . The emission is spatially and dynamically resolved with a highly asymmetric double-horned line profile as shown in Figure 1. Fitting a double Gaussian results in peak flux densities of  $75.3 \pm 2.6$  mJy and  $24.0 \pm 2.0$  mJy, and a FWHM of  $179 \pm 9$  km s<sup>−1</sup> and  $255 \pm 28$  km s<sup>−1</sup> for the two components, respectively. The peaks are separated by  $\Delta v_{\text{sep}} = 400 \pm 12$  km s<sup>−1</sup>. The total integrated line flux is  $24.1 \pm 2.3$  Jy km s<sup>−1</sup>.

We construct the zeroth order moment map, a red/blue channel map, and the first and second moment maps in Figure 2 using the  $uv$ -continuum subtracted data cube over a velocity range of  $\Delta v \sim 750$  km s<sup>−1</sup>. The higher-order moment maps are produced using unbinned channel maps with  $3\sigma$  clipping. The peak flux density is  $8.12 \pm 0.30$  Jy km s<sup>−1</sup> beam<sup>−1</sup> in the intensity map.

The deconvolved source size FWHM from fitting a two-dimensional Gaussian is  $5''.1 \pm 0''.72 \times 3''.72 \pm 0''.66$ , and thus, the emission is resolved over  $\sim 2.2$  beams. While

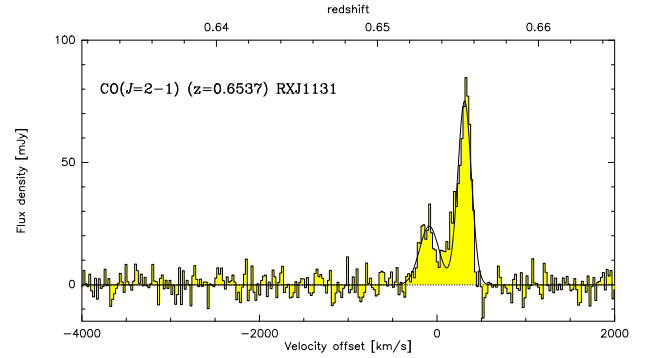


FIG. 1.— Continuum-subtracted spectrum of  $\text{CO}(J=2 \rightarrow 1)$  emission toward RXJ1131. The velocity scale is with respect to  $z=0.6537$ , which is approximately the line center considering the asymmetry resulting from differential lensing. A detailed discussion of this effect is presented in §5.1.2.

the lensed emission is not strictly distributed as a two-dimensional Gaussian; the fit recovers the line intensity enclosed by the emitting region, therefore we take this as an estimate on the full extent of the lensed emission. On the other hand, if we assume that the spatial distribution of the lensed molecular gas emission is similar to that in the optical to near-IR wavelengths, the lensed emission would be more accurately described by an annulus, enclosing the partially complete “Einstein ring” and the lensed knots (see Figure 2).

We also place an upper limit on  $\text{HNC}(J=2 \rightarrow 1)$  line emission in the foreground galaxy at  $z \sim 0.295$ . Assuming a typical line width of  $300$  km s<sup>−1</sup>, this corresponds to a  $3\sigma$  limit of  $0.35$  Jy km s<sup>−1</sup> beam<sup>−1</sup>.

### 4.2. $\text{CO}(J=3 \rightarrow 2)$ Emission

We detect  $\text{CO}(J=3 \rightarrow 2)$  line emission toward RXJ1131 in the CARMA data at  $\gtrsim 5\sigma$  significance. The spectrum is shown in Figure 3 and appears to be consistent with a double-peaked profile. We estimate a line intensity of  $35.7 \pm 21.9$  Jy km s<sup>−1</sup> by summing up fluxes over the FWZI linewidth used to infer the  $\text{CO}(J=2 \rightarrow 1)$  line intensity ( $\sim 700$  km s<sup>−1</sup>). Assuming the spatial extents of  $\text{CO}(J=2 \rightarrow 1)$  and  $\text{CO}(J=3 \rightarrow 2)$  is similar and therefore the emission is magnified by the same amount, the measured line intensities correspond to a brightness temperature ratio of  $r_{32} = T_{\text{CO}(J=3 \rightarrow 2)} / T_{\text{CO}(J=2 \rightarrow 1)} = 0.66 \pm 0.41$ . Taking into account the large phase errors associated with  $\text{CO}(J=3 \rightarrow 2)$ , this is consistent with thermalized excitation, as observed in other ULIRGs.

### 4.3. Continuum Emission

No 1.5 mm continuum emission is detected at the position of  $\text{CO}(J=3 \rightarrow 2)$  down to a  $3\sigma$  limit of  $2.49$  mJy beam<sup>−1</sup>. This is consistent with the spectrum shown in Figure 3.

We detect PdBI 2 mm continuum, as shown in Figure 4. The integrated flux density is  $1.2 \pm 0.2$  mJy, with a peak flux  $S_\nu = 800 \pm 88 \mu\text{Jy beam}^{-1}$  centered on the lensing galaxy. Slightly extended emission along the lensed arc is also detected. This suggests that we detect emission both in the foreground galaxy and in the background

<sup>1</sup> Based on observations made with the NASA/ESA Hubble Space Telescope, and obtained from the Hubble Legacy Archive, which is a collaboration between the Space Telescope Science Institute (STScI/NASA), the Space Telescope European Coordinating Facility (ST-ECF/ESA) and the Canadian Astronomy Data Centre (CADC/NRC/CSA).

<sup>2</sup> [http://hla.stsci.edu/hla\\_faqs.html](http://hla.stsci.edu/hla_faqs.html)



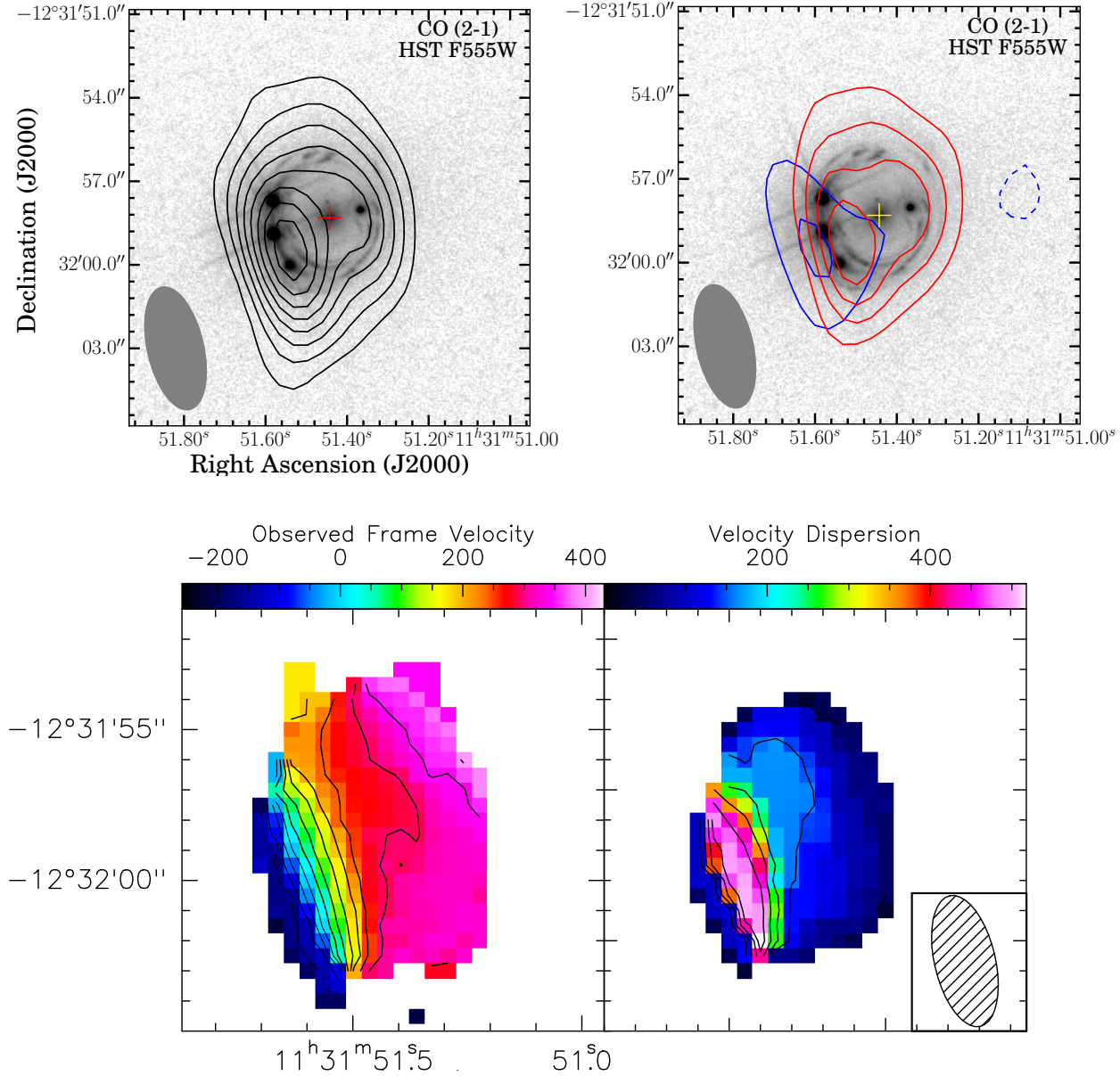


FIG. 2.— Top left: overlay of the velocity-integrated CO( $J=2 \rightarrow 1$ ) emission on the archival *HST* V-band (F555W) image. Top right: same as top left, except the contours are color-coded to represent the red- and blueshifted emission. The contours in both top panels start at  $3\sigma$  and increment at steps of  $\pm 3\sigma$ , where  $\sigma = 0.3 \text{ mJy beam}^{-1}$  for the top left panel, and  $\sigma = 0.4 \text{ mJy beam}^{-1}$  (red) and  $0.5 \text{ mJy beam}^{-1}$  (blue) for the top right panel. The crosses denote the location of the foreground galaxy at  $z=0.295$ . Contours for the first (bottom left) and second (bottom right) moment maps of the CO( $J=2 \rightarrow 1$ ) line emission are shown in steps of  $50 \text{ km s}^{-1}$ , and  $100 \text{ km s}^{-1}$ , respectively. The synthesis beam size is  $4''.4 \times 2''.0$ , at PA =  $13^\circ$ .

galaxy and that the emission is marginally resolved along its major axis. We subtract a point source model in the  $uv$ -plane to remove the unresolved emission toward the foreground galaxy. The peak flux ( $0.39 \pm 0.08 \text{ mJy}$ ) in the residual map coincides with the lensed arc, and is consistent with the difference between the integrated and the peak flux in the original continuum map ( $\sim 0.4 \text{ mJy}$ ). We therefore adopt  $S_\nu = 0.39 \pm 0.08 \text{ mJy}$  as the 2 mm continuum emission toward the background galaxy (RXJ1131).

The VLA C-band continuum image in Figure 4 shows resolved emission from the jets and the core of the foreground elliptical galaxy as well as emission toward the background quasar. Multiple peaks are seen along the arc with their centroids coincident with the optical emis-

sion from the quasar. We extract the flux densities for the lensing arc and the radio core in Table 1. We find a spectral index of  $\alpha_{6\text{cm}}^{2\text{mm}} = -0.024$  for the foreground galaxy and  $\alpha_{6\text{cm}}^{2\text{mm}} = -0.345$  for the background galaxy by fitting a power-law ( $S_\nu \propto \nu^\alpha$ ) to the continuum emission at 5 GHz and 2 mm.

#### 4.4. Photometry

We compile mid-IR (MIR) to far-IR broadband photometry from various catalogs available on the NASA/IPAC Infrared Science Archive (IRSA) in Table 1 with aperture corrections when warranted. These data were obtained using the Two Micron All Sky Survey Telescopes (2MASS; Skrutskie et al. 2006), the Wide-field Infrared Survey Ex-

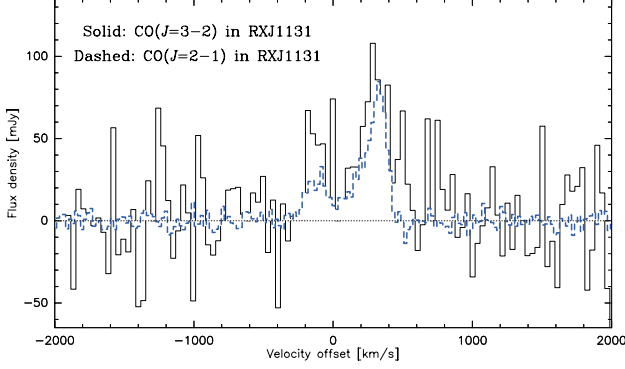


FIG. 3.— CARMA CO( $J=3 \rightarrow 2$ ) line profile (solid) without continuum subtraction is over-plotted on the continuum-subtracted PdBI CO( $J=2 \rightarrow 1$ ) line profile (dashed). The velocity scale is with respect to  $z=0.6537$ , which corresponds to the dynamical center of the CO( $J=2 \rightarrow 1$ ) line. The spectral resolution for CO( $J=3 \rightarrow 2$ ) and CO( $J=2 \rightarrow 1$ ) is  $35.8 \text{ km s}^{-1}$  and  $21.5 \text{ km s}^{-1}$ , respectively.

plorer (*WISE*; Wright et al. 2010), the *Infrared Astronomical Satellite* (*IRAS*; Neugebauer et al. 1984), and the Multi-band Imaging Photometer (*MIPS*; Rieke et al. 2004) and Mid-infrared Infrared Array Camera (*IRAC*; Fazio et al. 2004) on the *Spitzer Space Telescope*. We retrieve PBCD (level 2) *Spitzer*/IRAC images from the Spitzer Heritage Archive and perform aperture photometry on the channel 1 image to extract the flux density at  $3.6 \mu\text{m}$  since it is not available from the IRSA archive.

The emission in the IRAC images is slightly extended. We thus use an *HST* image ( $\sim 0''.07$  resolution) to determine the origins of their centroids, all of which are found to be centered at the position corresponding to the lensed emission from the background galaxy. To recover the diffuse background emission, we subtract a point source model centered on the lensing galaxy, using the average FWHM found by fitting a Gaussian profile to several field stars with the IMEXAM routine of IRAF. We perform aperture photometry on the residual image to obtain decomposed flux measurements of the background galaxy. The photometry for the foreground galaxy is then obtained by subtracting the background emission from the observed total flux. The resulting photometry in Table 1 is obtained after performing an aperture correction described in the IRAC Instrument Handbook<sup>3</sup> to correct for the fact that the imaging was calibrated using a  $12''$  aperture, which is larger than the aperture ( $5''.8$ ) we used to perform aperture photometry.

We fit a power-law spectrum to the decomposed IRAC photometry to disentangle the background and foreground emission from the total flux observed in the MIPS  $24 \mu\text{m}$  band. The spectral indices corresponding to the best-fitting curves are  $\alpha = -1.8$  and  $\alpha = -0.85$  for the lensing galaxy and RXJ1131, respectively. The latter is consistent with the mean  $3.6\text{--}8 \mu\text{m}$  spectral slope of  $\alpha = -1.07 \pm 0.53$  found for unobscured AGN (Stern et al. 2005). An extrapolation of the fit to  $24 \mu\text{m}$  yields  $33.96 \pm 0.01 \text{ mJy}$  and  $25.19 \pm 0.03 \text{ mJy}$  for the foreground galaxy and RXJ1131, respectively. The uncertainties are the standard deviations of the extrapolated fluxes obtained from two inde-

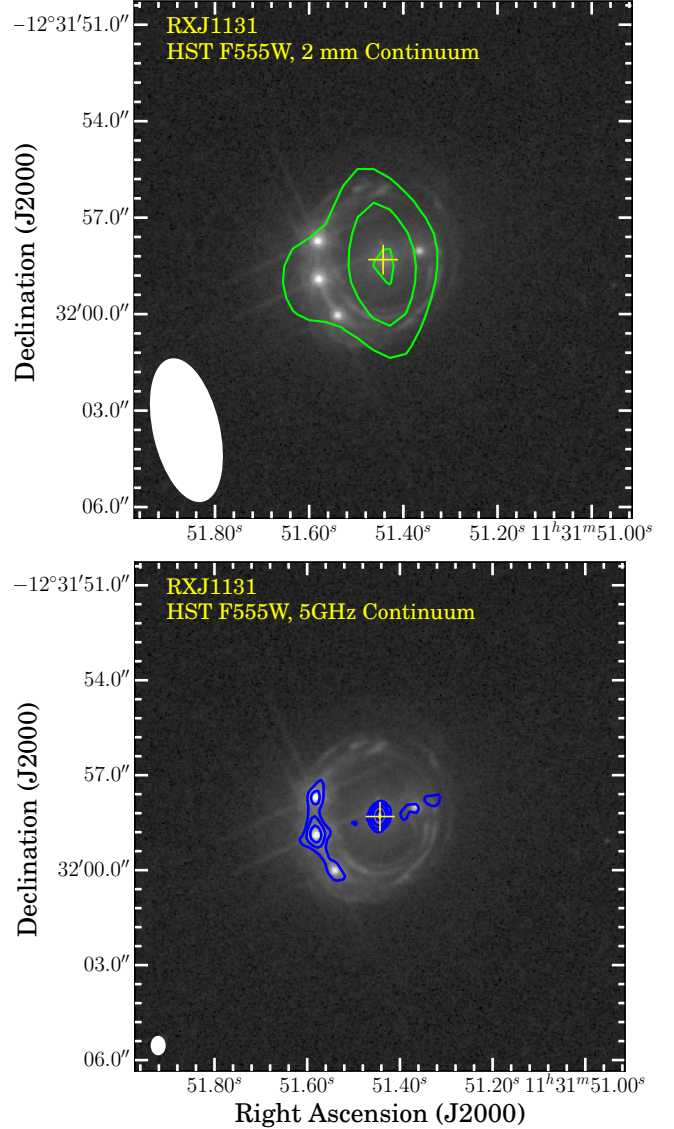


FIG. 4.— Top: overlay of the 2 mm continuum emission on the optical image. Bottom: overlap of the VLA 5 GHz continuum emission on the optical image. Contours in both images start and increment at steps of  $\pm 3\sigma$ , where  $\sigma_{2\text{mm}} = 0.082 \text{ mJy beam}^{-1}$  and  $\sigma_{5\text{GHz}} = 13 \mu\text{Jy beam}^{-1}$  in the top and bottom panel, respectively. The central crosses indicate the centroid of the foreground galaxy, as detected in the optical image. The synthesis beam size is  $4''.4 \times 2''.0$ , at PA =  $13^\circ$  for the PdBI observations (top), and  $0''.5 \times 0''.4$  (PA =  $0.18^\circ$ ) for the VLA observations (bottom).

pendent Monte Carlo simulations, each of 500 iterations. We incorporate the decomposed  $24 \mu\text{m}$  data in our SED fitting to provide some constraints on the Wien tail beyond the dust peak of the spectral energy distribution (SED) of RXJ1131. Details of the SED modeling are presented in §5.4.

Extraction of the *Herschel*/SPIRE photometry at 250, 350, and  $500 \mu\text{m}$  was carried out using SUSSEXTRACTOR within the Herschel Interactive Processing Environment (HIPE; Ott 2010) on Level 2 maps obtained from the Herschel Science Archive. These maps were processed by the SPIRE pipeline version 13.0 within HIPE. The SUSSEXTRACTOR task estimates the flux density from an image convolved with a kernel derived from the SPIRE beam.

<sup>3</sup> <http://irsa.ipac.caltech.edu/data/SPITZER/docs/irac/iracinstrumenthandbook/>

TABLE 1  
PHOTOMETRY DATA

Wavelength $\mu\text{m}$	Frequency GHz	Flux Density mJy	Instrument
Combined/Unresolved			
1.25	239834	$1.009 \pm 0.09$	2MASS/J-Band
1.65	181692	$1.448 \pm 0.12$	2MASS/H-Band
2.17	138153	$2.064 \pm 0.16$	2MASS/Ks-Band
3.4	88174.2	$7.027 \pm 0.14$	WISE/W1
3.6	83275.7	$5.618 \pm 0.0021$	Spitzer/IRAC
4.5	66620.5	$7.803 \pm 0.0021$	Spitzer/IRAC
4.6	65172.3	$8.872 \pm 0.16$	WISE/W2
5.8	51688.4	$10.720 \pm 0.0051$	Spitzer/IRAC
8.0	37474.1	$14.470 \pm 0.0041$	Spitzer/IRAC
12	24982.7	$21.960 \pm 0.42$	WISE/W3
12	24982.7	$< 400$	IRAS
22	13626.9	$55.110 \pm 1.9$	WISE/W4
24	12491.4	$70.204 \pm 0.026$	Spitzer/MIPS
25	11991.7	$< 500$	IRAS
60	4996.54	$< 600$	IRAS
100	2997.92	$< 1000$	IRAS
250	1199.17	$289.4 \pm 9.6$	Herschel/SPIRE
350	856.55	$168.2 \pm 8.6$	Herschel/SPIRE
500	599.585	$56.8 \pm 8.8$	Herschel/SPIRE
1387.93	216	$< 2.492$	CARMA
2152.82	139.256	$1.230 \pm 0.220$	PdBI
Foreground Lensing Galaxy (deblended bands)			
0.555	540167	$0.056 \pm 0.006$	HST-ACS/V-Band
0.814	368295	$0.238 \pm 0.013$	HST-ACS/I-Band
1.6	187370	$0.539 \pm 0.041$	HST-NICMOS(NIC2)/H-Band
3.6	83275.7	$0.585 \pm 0.003^a$	Spitzer/IRAC
4.5	66620.5	$1.794 \pm 0.0027^a$	Spitzer/IRAC
5.8	51688.4	$3.163 \pm 0.0059^a$	Spitzer/IRAC
8.0	37474.1	$4.589 \pm 0.0057^a$	Spitzer/IRAC
2152.82	139.256	$0.799 \pm 0.082$	PdBI
61414	4.8815	$0.866 \pm 0.027$	VLA
Background Galaxy RXJ1131 (deblended bands)			
0.555	540167	$0.009 \pm 0.0041^b$	HST-ACS/V-Band
0.814	368295	$0.041 \pm 0.0054^b$	HST-ACS/I-Band
1.6	187370	$0.133 \pm 0.004^b$	HST-NICMOS(NIC2)/H-Band
3.6	83275.7	$5.034 \pm 0.0021$	Spitzer/IRAC
4.5	66620.5	$6.009 \pm 0.0017$	Spitzer/IRAC
5.8	51688.4	$7.557 \pm 0.003$	Spitzer/IRAC
8.0	37474.1	$9.881 \pm 0.0039$	Spitzer/IRAC
2152.82	139.256	$0.400 \pm 0.082^c$	PdBI
61414	4.8815	$1.273 \pm 0.042$	VLA

REFERENCES. — The *HST* photometry is taken from C06.

NOTE. — The IRAC photometry for channel 1 (3.6  $\mu\text{m}$ ) is extracted directly from the image and from the Spitzer Heritage Archive for channels 2–4 (4.5, 5.8, and 8.0  $\mu\text{m}$ ). All upper limits are  $3\sigma$ .

<sup>a</sup> Flux obtained using aperture photometry after subtracting the emission of RXJ1131 from the total emission.

<sup>b</sup> A contribution from the quasar has been removed (see C06), and thus the flux density corresponds to the host galaxy only.

<sup>c</sup> Flux extracted from the residual map after subtracting a point-source model.

The flux density measured by SUSSEXTRACTOR is additionally confirmed using the Timeline Fitter, which performs photometry by fitting a 2D elliptical Gaussian to the Level 1 data at the source position given by the output of SUSSEXTRACTOR. The fluxes obtained from both methods are consistent within the uncertainties.

## 5. ANALYSIS

### 5.1. Lens Modeling

At the angular resolution of the CO( $J=2 \rightarrow 1$ ) data, the images are resolved over  $\sim 2$  resolution elements. Given

the extent of the lensed emission (see Figure 2), this implies that we do not resolve structures (e.g. knots and arcs) of the lensed emission in our CO( $J=2 \rightarrow 1$ ) data. Nevertheless, the high spectral resolution of these data provides dynamical information on spatial scales smaller than the beam (see Figure 2). Hence, we reconstruct the intrinsic gas dynamics by carrying out a parametric lens modeling over different channel slices of the interferometric data using our lensing code UVMCMCFIT (Bussmann et al. 2015a; see Bussmann et al. 2015b for details of the code). Models of each slice thus provide information on the corresponding kinematic component of the CO gas, enabling us to reconstruct a velocity gradient in the source plane. To ensure adequate SNRs for lens modeling, we bin the frequency channels by a factor of five to produce seven independent  $\Delta v \sim 105 \text{ km s}^{-1}$  channels (dashed line in Figure 5) that cover the full linewidth of  $\sim 750 \text{ km s}^{-1}$ .

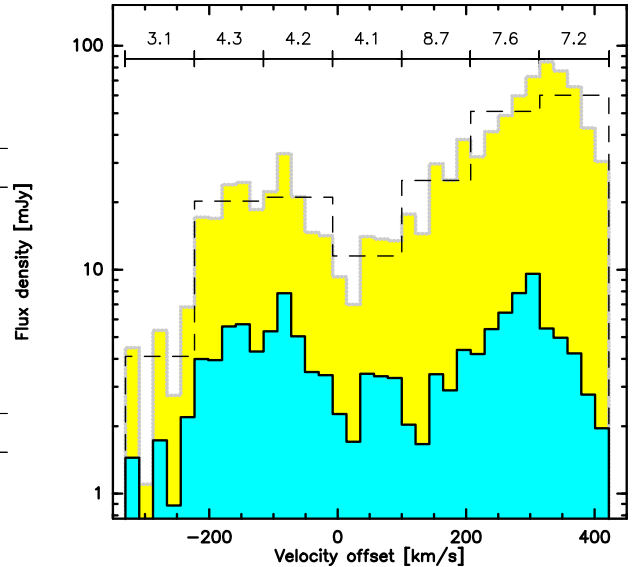


FIG. 5.— The full resolution CO( $J=2 \rightarrow 1$ ) spectrum (yellow histogram) and the binned spectrum (dashed line) with the seven  $\Delta v \sim 105 \text{ km s}^{-1}$  channels used for lens modeling. The blue histogram shows the “intrinsic” line profile of RXJ1131 after subtracting a contribution from its companion galaxy and correcting for lensing using the magnification factor  $\mu_L$  as annotated by the horizontal bar shown above each respective model channel. Flux density on the y-axis is shown on a log scale.

The lens mass distribution is modeled using a singular isothermal ellipsoid (SIE) profile, which is described by five free parameters: the positional offset in R.A. and Dec. relative to an arbitrary chosen fixed coordinate in the image, the Einstein radius, the axial ratio, and the position angle. We use the VLA radio continuum emission toward the foreground galaxy to initialize the positional offset. We impose a uniform prior of  $\pm 0''.05$  in both  $\Delta \text{R.A.}$  and  $\Delta \text{Dec.}$ , motivated by the astrometry uncertainties in the VLA image as well as the uncertainties provided by previous SIE lens model (C06). We initialize the Einstein radius based on the model parameters reported by C06 and impose a uniform prior using  $\pm 3\sigma$  of their uncertainties. The sources are modeled using elliptical Gaussian profiles, which are parameterized by six free parameters: the positional offset in R.A. and Dec. relative to the lens, the in-



TABLE 2  
LENS PARAMETERS CONSTRAINED BY  
MODELS OF SEVEN VELOCITY CHANNELS

Parameters		Median values
Offset in RA	( $''$ )	$0.004 \pm 0.027$
Offset in Dec	( $''$ )	$0.003 \pm 0.027$
Axial Ratio		$0.56 \pm 0.16$
Position Angle	(deg)	$103 \pm 22$
Einstein Radius	( $''$ )	$1.833 \pm 0.002$

NOTE. — Parameters describing the foreground lens are obtained based on the median in the preliminary models (see text for details). All angular offsets are with respect to  $\alpha = 11^{\text{h}}31^{\text{m}}51^{\text{s}}.44$ ,  $\delta = -12^{\circ}31'58''.3$  (J2000).

trinsic flux density, the effective radius, the axial ratio, and the position angle. The position of each source is allowed to vary between  $\pm 1''.5$  (i.e., within the Einstein radius) and the effective radius is allowed to vary from  $0''.01$ – $2''$ .

Our code uses an Markov Chain Monte Carlo (MCMC) approach to sample the posterior probability distribution function (PDF) of the model parameters. In each model, we require a target acceptance rate of  $\sim 0.25$ – $0.5$  and check for chain convergence by inspecting trace plots and by requiring the samples are obtained beyond at least an autocorrelation time. We thus employ  $\sim 50,000$  samples as the initial “burn-in” phase to stabilize the Markov chains (which we then discard) and use the final  $\sim 5,000$  steps, sampled by 128 walkers, to identify the posterior. Here, we identify the best-fit model and the quoted uncertainties using the median and the 68% confidence intervals in the marginal PDFs.

We first obtain a preliminary lens model for each channel slice independently, where their lens parameters are allowed to vary and are initialized according to the aforementioned way. We obtain the final model by repeating the modeling over each slice but fixing their lens parameters to the overall median in the preliminary models, as listed in Table 2. This ensures that all models share the same lens profile. The magnification factors in Table 3 are determined by taking the ratio between the image plane flux and the source plane flux of each model.

Our model parameters in Table 2, describing the mass distribution of the lensing galaxy, are consistent (within the uncertainties) with that of the SIE model presented by C06. We find a mass of  $M(\theta < \theta_E) = (7.47 \pm 0.02) \times 10^{11} M_{\odot}$  within the Einstein radius.

#### 5.1.1. Interpretation of the Source-plane Morphology

The reconstructed source locations, as represented by magenta ellipses in Figure 6, demonstrate an intrinsic velocity gradient across the source plane, which is consistent with a kinematically-ordered disk-like galaxy. Additional support to the disk conjecture can be found in the double-horned line profile (Figure 1) and the observed (image plane) velocity field (Figure 2). Furthermore, C06 also find that the reconstructed source plane emission in optical-NIR is best-reproduced using a  $n = 1$  Sersic profile. We thus interpret RXJ1131 as a disk galaxy.

A better fit is found for the lens model of the red-most

channel if we add a second source component (see top left panel in Figure 6). This is consistent with previous results reported by Brewer & Lewis (2008, hereafter B08), who find an optically faint companion (component F in their paper)  $\sim 2.4$  kpc in projection from the AGN host galaxy in V-band, and with C06, who find evidence for an interacting galaxy near RXJ1131. Spatially, the red velocity component of the CO emission also coincides with this component F. It is therefore likely that we detect CO( $J = 2 \rightarrow 1$ ) emission in a companion galaxy.

The type of merger (major v.s. minor) in a pair of interacting galaxies is most commonly distinguished based on the ratio between their total galaxy mass. Here, we use the gas mass ratio between RXJ1131 and its companion galaxy instead, given that we do not have stringent constraints on their individual galaxy mass. We decompose the total line flux into two components: one from RXJ1131 and the other from its companion. Since the companion is only detected in the red-most channel, we derive its intrinsic gas mass using the best-fit flux densities and magnification factors obtained from the models of this channel. Assuming a brightness temperature ratio of  $r_{21} = 1$  between CO( $J = 2 \rightarrow 1$ ) and CO( $J = 1 \rightarrow 0$ ) lines and a CO luminosity-to- $H_2$  mass conversion factor of  $\alpha_{\text{CO}} = 0.8 M_{\odot} (\text{K km pc}^2)^{-1}$ , we find a molecular gas mass of  $M_{\text{gas}} = (1.92 \pm 0.09) \times 10^9 M_{\odot}$ . For the molecular gas mass in RXJ1131, we derive its intrinsic line flux over the FWZI linewidth using the respective magnification factors listed in Table 3, which to first order takes into account the effect of differential lensing. This yields  $I_{\text{CO}(J=2 \rightarrow 1)} = 2.93 \pm 0.70 \text{ Jy km s}^{-1}$ , where the uncertainty includes those on the magnification factors. Adopting the same brightness temperature ratio and  $\alpha_{\text{CO}}$  as used for the companion, this corresponds to a gas mass of  $M_{\text{gas}} = (1.38 \pm 0.33) \times 10^{10} M_{\odot}$ , which implies a gas mass ratio of  $\sim 7:1$  between RXJ1131 and its companion. We thus classify the system to be a “wet” minor merger. We caution that this is based on their gas mass ratio rather than their total galaxy mass ratio, which is more commonly used in literature as the classification scheme to separate major mergers from minor mergers.

The spatial resolution of the data in hand is a few arcsec, which implies that despite the high SNR and spectral resolution, constraints on the intrinsic sizes of the lensed galaxies are modest, and thus the magnification factors may be under-predicted.

#### 5.1.2. Spatial Extent and Differential Lensing

In the image-plane integrated line map shown in Figure 2, the redshifted component is cospatial with the Einstein ring seen in the optical image, with most of its apparent flux originating from the lensed arc in the south-east, whereas the blue component is predominately coming from solely the lensed arc. To further illustrate this, we show the channel maps of  $21.5 \text{ km s}^{-1}$  width and a spatial spectra map of  $1''.5$  resolution in Figure 7 and Figure 8, respectively. The figures show that redshifted emission is present to the west, peaking toward the lensing arc (black crosses in Figure 7), and shifts to the east with decreasing

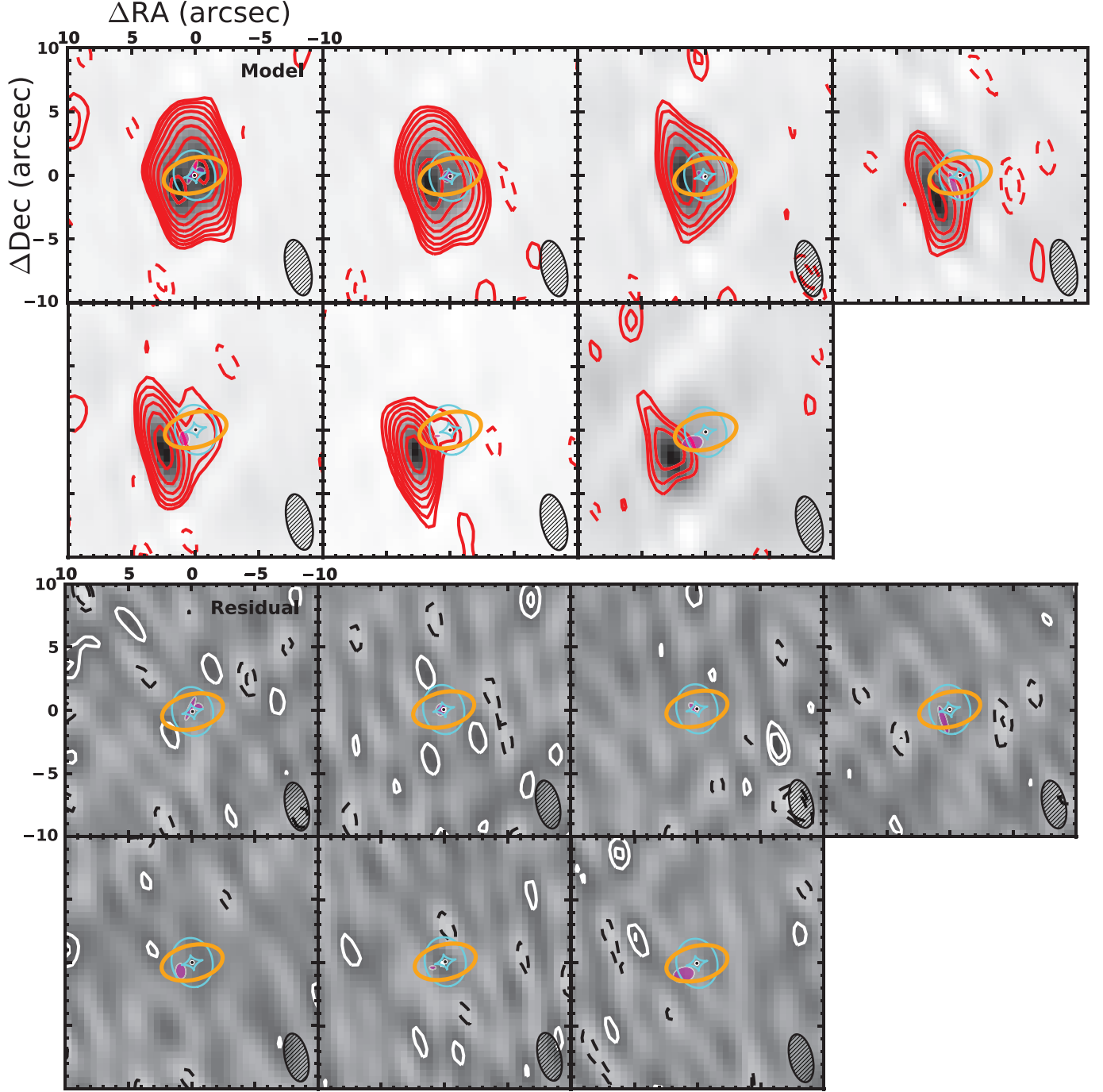


FIG. 6.— Best-fit lens models of the PdBI CO( $J=2 \rightarrow 1$ ) data in different velocity channels, as listed in Table 3. Top: each panel corresponds to a channel map of width  $\sim 100 \text{ km s}^{-1}$  of the observed emission (red) overlaid on the best-fit models (grayscale). Bottom: residual images obtained by taking a Fourier transform after subtracting the best-fit model from the data in the  $uv$ -domain. In all panels, location of the foreground lensing galaxy is indicated by a black dot and its critical curve is traced by the orange solid line; locations and morphologies (half-light radii) of the reconstructed sources are represented by magenta ellipses; the caustic curves are represented as cyan lines. Contours start at  $\pm 3\sigma$  and increment at steps of  $3 \times 2^n \sigma$ , where  $n$  is a positive integer. The beam of the PdBI observations is shown in the bottom right corner. The reconstructed source-plane positions, as represented by the magenta ellipses, demonstrate an intrinsic velocity gradient of the CO( $J=2 \rightarrow 1$ ) emission in RXJ1131. The best-fit model of the red-most channel (top left panel) contains two source components (see text for details).



TABLE 3  
MAGNIFICATION FACTORS OF VARIOUS KINEMATIC  
COMPONENTS IN CO( $J=2 \rightarrow 1$ )

Velocity Range (km s <sup>-1</sup> )	Source 1 $\mu_L$	Source 2 $\mu_L$
-366 – -258	$3.1 \pm 0.9$	
-237 – -151	$4.3 \pm 2.4$	
-129 – -43	$4.2 \pm 0.6$	
-21.5 – 65	$4.1 \pm 0.9$	
86 – 172	$8.7 \pm 2.0$	
194 – 280	$7.6 \pm 1.6$	
301 – 388	$7.2 \pm 5.6$	$6.7 \pm 2.5$
weighted average	4.4	
median	5.5	

NOTE. — Velocity is taken from the center of each (native) channel without any binning. Each row corresponds to a channel slice used for lens modeling. Source 1 is RXJ1131 and source 2 is its companion. See text for details.

velocity (blue wing). This is consistent with the source plane positions in our models and is suggestive of an extended CO emitting region.

Similar to previous studies of RXJ1131, where differential lensing across *HST* V-, I-, and H-band has been detected with a magnification factor decreasing from 10.9 to 7.8 (C06), the highly asymmetric CO( $J=2 \rightarrow 1$ ) line profile suggests that differential lensing is also non-negligible for CO, causing the redshifted emission to be apparently much brighter than the blueshifted component. This can be explained by the difference in magnification factor ( $\mu_L$ ) which varies from 8.7 to 3.1 across the CO( $J=2 \rightarrow 1$ ) line (Table 3) and also partly due to a contribution from the companion in the redshifted velocity channels. The variation in  $\mu_L$  across channels is consistent with the source plane positions relative to the caustics in Figure 6, where the red wing emission mainly originates near the cusp of the caustic and the blue wing emission is located beyond the caustics. In fact, the intrinsic line flux of the redshifted and blueshifted emission in RXJ1131 (after subtracting a contribution from the companion) are  $I_{\text{CO}(J=2 \rightarrow 1)} = 1.26 \pm 0.23$  Jy km s<sup>-1</sup> and  $1.25 \pm 0.23$  Jy km s<sup>-1</sup>, respectively, implying an intrinsically symmetric line profile (Figure 5). This is consistent with the symmetric source-plane velocity gradient in our lens model (Figure 6 and Figure 9).

### 5.2. CO( $J=2 \rightarrow 1$ ) Kinematics

Fitting two Gaussians with a single FWHM to the “intrinsic” CO( $J=2 \rightarrow 1$ ) line profile of RXJ1131 (after correcting for lensing using the magnification factors for various channels and separating the emission from RXJ1131 and its companion), we find a roughly symmetric double-horned profile with a flux ratio of  $1.2 \pm 0.4$  between the peaks, which are separated by  $\Delta v_{\text{sep}} = 387 \pm 45$  km s<sup>-1</sup>, and each with a FWHM of  $220 \pm 72$  km s<sup>-1</sup>. The peak separation obtained from this “intrinsic” line profile is slightly lower than that obtained from the observed spectrum (i.e., without lensing corrections). This discrepancy is likely a result of differential lensing, which causes the line peak of the red wing to shift towards higher velocity channels, and thereby biasing the centroid of one Gaus-

sian to higher velocity than otherwise. To facilitate a comparison (§5.5.1) with previous works, which were observed at lower spectral resolution, we also fit a single-Gaussian to the intrinsic line profiles. This yields FWHMs of  $600 \pm 160$  km s<sup>-1</sup> for RXJ1131 and  $73 \pm 43$  km s<sup>-1</sup> for the companion galaxy.

A clear velocity gradient and a high velocity dispersion ( $\gtrsim 400$  km s<sup>-1</sup>) near the central region is seen in Figure 2. While beam smearing is inevitably the dominant factor in the observed velocity dispersion at the spatial resolution of these data, the exceedingly high velocity dispersion may hint at potential perturbations from the AGN, or internal turbulence due to interactions with the companion, and/or instability due to the large gas content. Therefore, in this scenario, RXJ1131 is consistent with a disrupted disk galaxy hosting an optically bright quasar and in the process of merging.

### 5.3. CO( $J=2 \rightarrow 1$ ) Dynamical Modeling

Assuming the velocities of the respective channels used in the lens modeling correspond to solely the tangential component of the true velocity vector of a rotating disk (i.e., along the major axis), we extract a one dimensional PV diagram in Figure 9 by slicing across their source plane positions (PA: 121°).

We then attempt to characterize the molecular gas kinematics using an empirically-motivated disk model (e.g., Courteau 1997; Puech et al. 2008; Miller et al. 2011):

$$V = V_0 + \frac{2}{\pi} V_a \arctan\left(\frac{R}{R_t}\right), \quad (1)$$

where  $V$  is the observed velocity,  $V_0$  is the velocity at dynamical center,  $V_a$  is the asymptotic velocity, and  $R_t$  is the “turnover” radius at which the rising part of the curve begins to flatten. We perform non-linear least square fitting using an orthogonal distance regression to find the best-fit parameters, taking into account the uncertainties in both velocity (channel width) and distance offset. We also place an upper limit on  $R_t < 15$  kpc to keep this parameter physical (e.g., Puech et al. 2008; Miller et al. 2011). The parameter uncertainties are inferred based on a Monte Carlo simulation of 500 iterations, where the input parameters are perturbed according to random Gaussian distributions with standard deviations corresponding to their uncertainties. Using this model, we find  $V_a = 975 \pm 387$  km s<sup>-1</sup>,  $R_t = 10.7 \pm 5.7$  kpc, and  $V_0 = 28 \pm 40$  km s<sup>-1</sup>. However, since the emission is not resolved along the flat regime of the rotation curve, the asymptotic velocity and the “turnover” radius are poorly constrained. In particular,  $V_a$  and  $R_t$  are highly correlated with a Pearson coefficient  $R = 0.998$ , and 0.027 between  $V_a$  and  $V_0$ .

The asymptotic velocity ( $V_a$ ) — an extrapolation of the model out to radius beyond the disk scale-length and half-light radius — is not equivalent to the maximum observed velocity ( $V_{\text{max}}$ ), which is commonly used in literature to parameterize disk rotation. The arctangent model is most commonly used in studies of the Tully-Fisher relation, where an extrapolation to  $V_{2.2}$  (velocity at 2.2 disk scale-

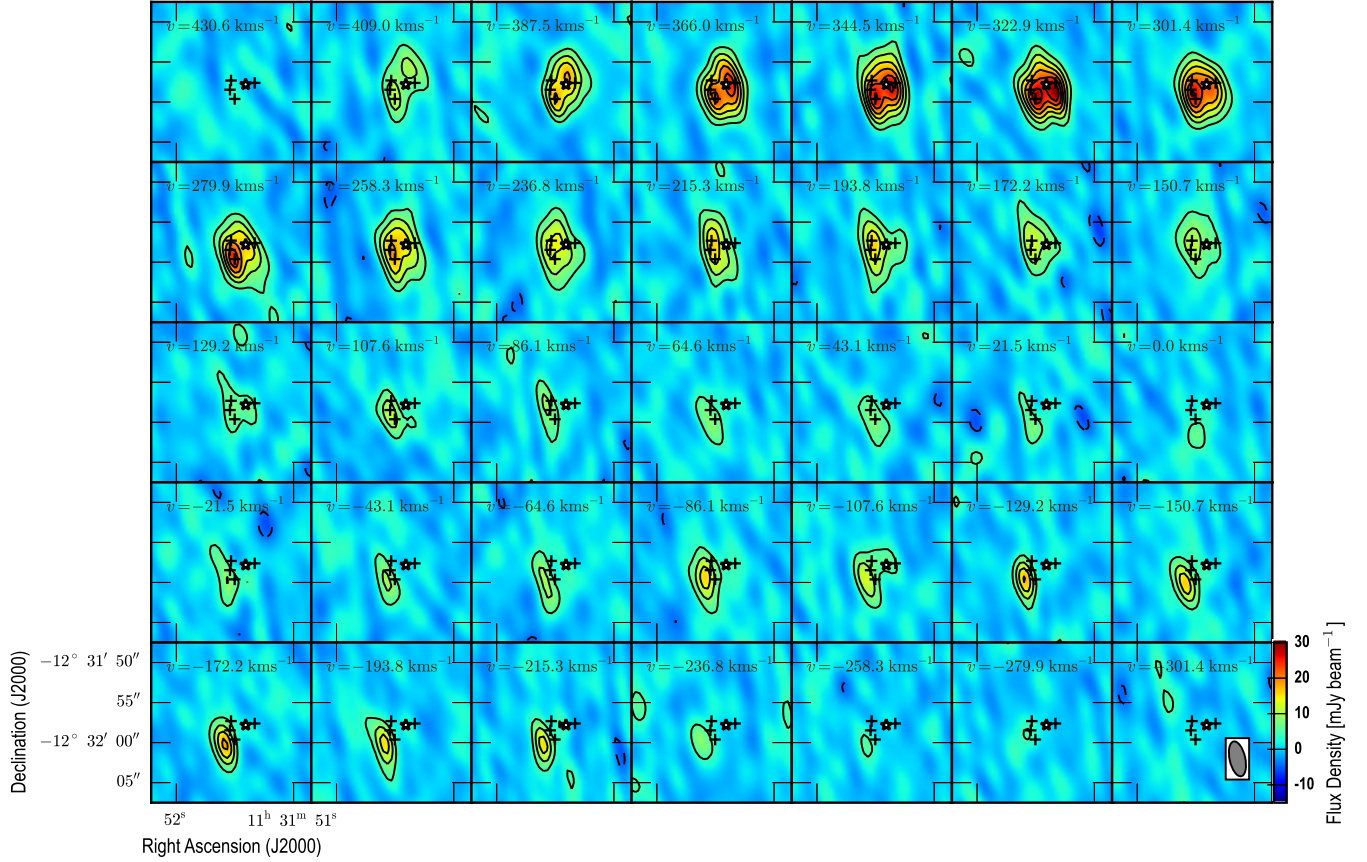


FIG. 7.— Channel maps of the PdBI CO( $J=2 \rightarrow 1$ ) data cube toward RXJ1131 at  $21.5 \text{ km s}^{-1}$  resolution. Black crosses indicate the positions of the lensed knots (AGN emission, which correspond to components ABCD in C06). The central white-filled star indicates the position of the foreground lensing galaxy (component G in C06). Central velocities are shown at the top of each map. Contours start and increment at steps of  $\pm 3\sigma$ . The beam is denoted in the bottom right panel.

length or  $\sim 1.375$  half-light radius, or  $\sim 0.7R_{\text{opt}}^4$ ) is typically adopted as the rotation velocity ( $V_{\text{max}}$  in their terminology) since this corresponds to the radius at which the velocity of a pure exponential disk peaks (Courteau & Rix 1997). Here, we adopt the maximum observed velocity  $V_{\text{rot}} = 345 \pm 55 \text{ km s}^{-1}$  at  $6 \pm 3 \text{ kpc}$  from the dynamical center as a proxy to the rotation velocity. This radius corresponds to  $\sim 0.6 R_e$ , where  $R_e$  is the half-light radius  $\sim 10.3 \text{ kpc}$  inferred from the *HST* *I*-band lens model (C06; converted to our cosmology). We note that the source plane half-light radius varies substantially with wavelength. In particular, the half-light radius is found to be  $\sim 4 \text{ kpc}$  and  $\sim 7 \text{ kpc}$  in *V*-band (B08) and *H*-band (C06), respectively. The CO gas is thus of similar spatial extent as in *H* and *I*-bands.

In the rest-frame, emission in the observed-frame *H*-band corresponds to NIR emission ( $\sim 1 \mu\text{m}$ ), tracing radiation from the accretion disk surrounding the central AGN and also from old and evolved stellar populations; *I*-band corresponds to roughly the optical *V*-band, tracing stellar radiation from existing, less massive (i.e., longer-lasting) stars; *V*-band corresponds to roughly *U*-band, tracing radiation from massive young stars in the host galaxy. Hence, the *V*-band compactness may be explained in part due to

the fact that its emission is more susceptible to dust extinction than in other bands and/or a central starburst caused by higher concentrations of star-forming gas towards the central regions — owing to gravitational perturbations induced from interactions with the companion (e.g., Di Matteo et al. 2005). This is consistent with the picture that old stars form first and constitute the bulge component of a spiral galaxy and that nuclear starbursts (in the inner few kpc) can be triggered at a later time as the progenitor disk galaxy interacts with other galaxies to form a larger bulge.

#### 5.4. SED Modeling

We fit dust SED models to the  $24 \mu\text{m}$ – $2.2 \text{ mm}$  photometry using a modified-blackbody (MBB) function with a power-law attached to the Wien side to account for the MIR excess due to emission of warm and small dust grains. The IRAS  $60 \mu\text{m}$  and  $100 \mu\text{m}$  upper limits are included to constrain the dust peak. The fit is performed using the code MBB\_EMCEE (e.g., Riechers et al. 2013; Dowell et al. 2014), which samples the posterior distributions using an MCMC approach and uses instrumental response curves to perform color correction. The model is described by five free parameters: the rest-frame characteristic dust temperature ( $T_d$ ), the emissivity index ( $\beta$ ), the power-law index ( $\alpha$ ), the flux normalization at  $500 \mu\text{m}$  ( $f_{\text{norm}}$ ), and the observed-frame wavelength at which the

<sup>4</sup> Radius enclosing 83% of the light distribution.

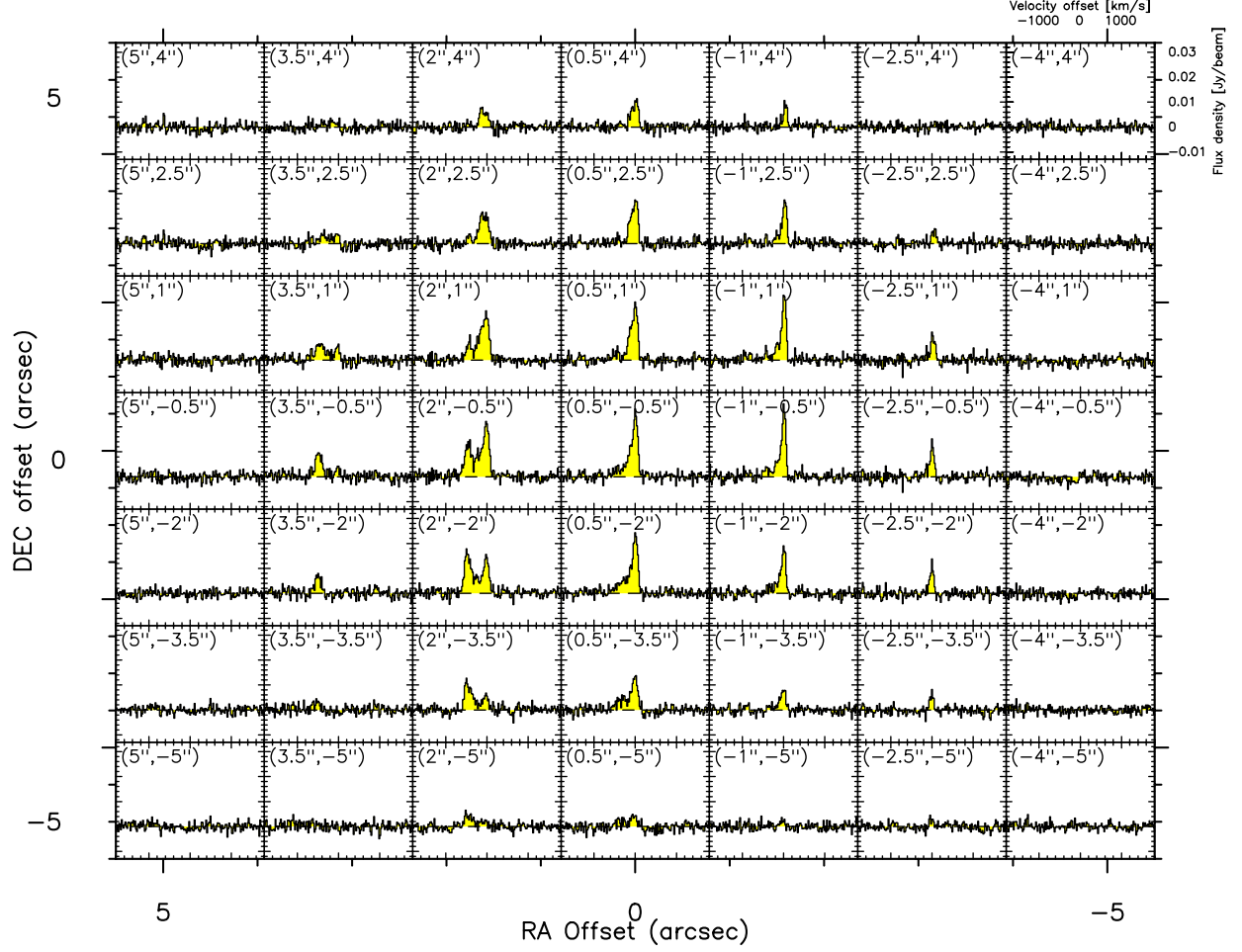


FIG. 8.— CO( $J=2 \rightarrow 1$ ) spectrum as a function of position, binned by 3 pixels in each direction ( $1''.5$ ). The spectra map covers an extent of  $\sim 10'' \times 10''$  centered on the pixel that corresponds to coordinates of the lensing galaxy ( $\alpha_{J2000} = 11^h 31^m 51^s.44$ ,  $\delta_{J2000} = -12^\circ 31' 58''.3$ ). Spatial offset in arcsec is denoted in top left corner of each panel. The velocity and flux density scales are denoted in the top right panel.

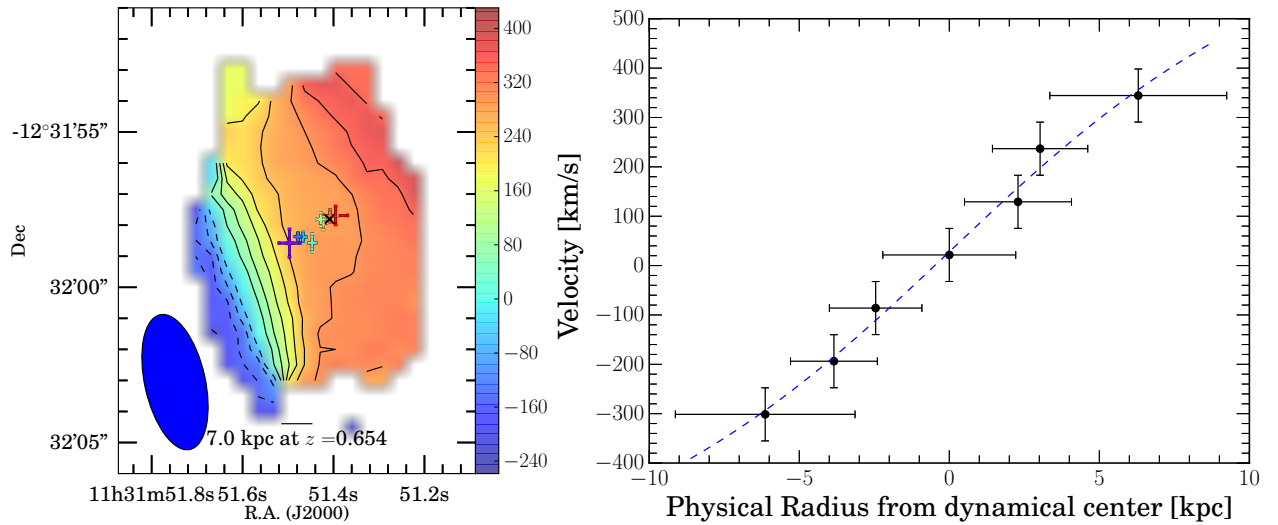


FIG. 9.— Left: Source-plane positions from best-fit CO( $J=2 \rightarrow 1$ ) lens models are indicated with their associated uncertainties atop the observed first moment map. The contours are at steps of  $50 \text{ km s}^{-1}$ . Right: PV slice along the major axis in the source plane at  $\text{PA} = 121^\circ$ . Dashed line shows the best-fit rotation curve using an arctangent model. The vertical error bars show the channel width for each model and the horizontal error bars are the  $1\sigma$  uncertainties on the source plane positions.



TABLE 4  
SED FITTING RESULTS

Parameters		With 24 $\mu$ m	Without 24 $\mu$ m
$T_d$	(K)	$52.0^{+4.0}_{-4.1}$	$58.2^{+14.5}_{-14.4}$
$\beta$		$1.8^{+0.5}_{-0.6}$	$2.1^{+0.3}_{-0.3}$
$\alpha$		$1.6^{+0.5}_{-0.5}$	$8.9^{+6.9}_{-6.3}$
$\lambda_0^a$	( $\mu$ m)	$548^{+285}_{-307}$	$367^{+125}_{-145}$
$\lambda_{\text{peak}}^b$	( $\mu$ m)	$162^{+16}_{-30}$	$146^{+39}_{-44}$
$f_{\text{norm}, 500\mu\text{m}}^c$	(mJy)	$59^{+14}_{-13}$	$60^{+5}_{-5}$
$L_{\text{FIR}}^d$	( $10^{12} L_\odot$ )	$3.81^{+2.04}_{-1.92}$	$4.72^{+2.54}_{-2.26}$
$M_d^e$	( $10^8 M_\odot$ )	$22^{+5}_{-18}$	$11^{+5}_{-6}$

NOTE. — Errors reported here are  $\pm 1\sigma$ .  $L_{\text{FIR}}$  and  $M_d$  are not corrected for lensing.

<sup>a</sup> Observed-frame wavelength where  $\tau_\nu = 1$

<sup>b</sup> Observed-frame wavelength of the SED peak

<sup>c</sup> Observed-frame flux density at 500  $\mu$ m

<sup>d</sup> Rest-frame 42.5–122.5  $\mu$ m luminosity

<sup>e</sup> Derived assuming absorption mass coefficient of  $\kappa = 2.64 \text{ m}^2 \text{ kg}^{-1}$  at  $\lambda = 125.0 \mu\text{m}$  (Dunne et al. 2003)

emission becomes optically thick ( $\lambda_0$ ). We impose a uniform prior with an upper limit of 100 K on  $T_d$  (see e.g., Sajina et al. 2012), a Gaussian prior centered around 1.9 with a standard deviation of 0.3 on  $\beta$ , and a uniform prior with an upper limit of 1000  $\mu$ m on  $\lambda_0$ . We check for chain convergence by requiring that the autocorrelation length of each parameter is less than the number of steps taken for the burn-in phase (which are then discarded). Here we report the statistical means and the  $1\sigma$  confidence interval in the marginal PDFs as the best-fit parameters, as listed in Table 4. The best-fit models are shown in Figure 10 along with the broadband photometry that are listed in Table 1.

In the first model, we attempt to constrain the power-law index by including the 24  $\mu$ m data. Based on the resulting posterior PDFs, we find an apparent far-IR luminosity (rest-frame 42.5–122.5  $\mu$ m) of  $3.81^{+2.04}_{-1.92} \times 10^{12} L_\odot$  and a dust mass of  $22^{+5}_{-18} \times 10^8 M_\odot$ , uncorrected for lensing. For the mass absorption coefficient, we adopt  $\kappa = 2.64 \text{ m}^2 \text{ kg}^{-1}$  at rest-frame 125.0  $\mu$ m (Dunne et al. 2003). The dust mass uncertainty does not include that of the absorption coefficient.

A fit including the MIR 24  $\mu$ m photometry is likely an upper limit on the far-IR luminosity due solely to star formation in the AGN host galaxy. If we instead fit for a model excluding this constraint, two major consequences are immediately apparent. First, the power-law index is poorly-constrained (see Table 4). Second, the steep power-law implies only a small contribution from the power-law regime to the total IR luminosity as compared to the graybody component. Thus, the far-IR luminosity in this model should, in principle, correspond to a lower limit on the cold dust emission. Using the best-fit parameters for this model, we find a total IR luminosity  $L_{\text{IR}}$  (rest-frame 8–1000  $\mu$ m) of  $9.71^{+6.14}_{-6.05} \times 10^{12} L_\odot$ , a far-IR luminosity  $L_{\text{FIR}}$  of  $4.72^{+2.54}_{-2.26} \times 10^{12} L_\odot$  and a dust mass  $M_{\text{dust}}$  of  $11^{+5}_{-6} \times 10^8 M_\odot$ , all of which are uncorrected for lensing. Taken at face value, this implies an FIR-to-IR luminosity ratio of  $\sim 58 \pm 35\%$ .

The dust temperature from both models is similar to that of ULIRGs at  $0.6 < z < 1.0$  ( $54 \pm 5$  K; Combes et al. 2013, hereafter C13). We note the far-IR luminosity is comparable in both models, which is not surprising given the lack of constraints in the MIR. For the subsequent analysis, we adopt the physical quantities from the first model (i.e., with constraints at 24  $\mu$ m). The choice of SED model does not affect the derived star formation rate (SFR) given the similar far-IR luminosity. Yet, the dust mass is higher by a factor of  $\sim 2$  in the former but consistent within the uncertainties. We correct for lensing using the median magnification factor ( $\mu_L = 5.5$ ) from the CO lens models. This yields a  $L_{\text{FIR}}$  of  $(6.9 \pm 3.6) \times 10^{11} L_\odot$  and a total IR luminosity of  $\sim 1.5 \times 10^{12} L_\odot$ , implying RXJ1131 can be classified as an ULIRG. Assuming a Salpeter (1955) initial mass function (IMF), we find a  $\text{SFR}_{\text{FIR}}$  of  $120 \pm 63 M_\odot \text{ yr}^{-1}$  using a standard conversion (Kennicutt 1998).

We derive the stellar mass of RXJ1131 by fitting SED models to the rest-frame UV-to-mm photometry using the high- $z$  version of the MAGPHYS code (da Cunha et al. 2008, 2015). Two sets of stellar templates modeled using either the Bruzual & Charlot (2003) or the unpublished Charlot & Bruzual 2007 stellar population synthesis code are provided in the MAGPHYS package. We adopt the former set. To minimize contaminations from the quasar, we only fit to the *HST*, *Herschel*, and PdBI data, where both the *HST* and the PdBI 2 mm photometry are de-blended from the AGN (see bottom section of Table 1). The input photometry are corrected for lensing using their respective magnification factors to account for differential lensing. We thus find a stellar mass of  $M^* = 2.95^{+1.32}_{-0.86} \times 10^{10} M_\odot$ , which is the median value of the posterior probability distribution and the uncertainties are derived from the 16<sup>th</sup> and 84<sup>th</sup> percentiles. We note that the models are overfitted with a best-fit  $\chi^2 = 0.41$  which is unsurprising due to sparse sampling of the SED compare to the number of free parameters. The resulting dust mass and  $L_{\text{IR}}$  are consistent with those obtained from the MBB+power-law models within the uncertainties, albeit some differences in the assumptions behind the two methods. The consistency may be attributed to the large uncertainties arising from the lack of photometric constraints on the models and the fact that the best-fit parameters from the MBB method are similar to those of the MAGPHYS method.

### 5.5. ISM Properties

In this section, we derive the gas properties of the merging system based on CO( $J=2 \rightarrow 1$ ) and compare them with those reported by C13<sup>5</sup> — the largest sample of CO-detected ULIRGs at similar redshift ( $0.6 < z < 1.0$ ). Their results are based on unresolved CO( $J=2 \rightarrow 1$ ) and CO( $J=4 \rightarrow 3$ ) line observations with the IRAM 30-m single-dish telescope.

<sup>5</sup> The far-IR luminosity in C13 is derived based on 60  $\mu$ m and 100  $\mu$ m IRAS fluxes, and using a different definition of  $L_{\text{FIR}}$ : rest-frame 40–500  $\mu$ m. Following this convention, we find a far-IR luminosity of  $L_{\text{FIR}} = (8.8 \pm 0.4) \times 10^{11} (\mu_L/5.5)^{-1} L_\odot$  and a SFR of  $(150 \pm 70) M_\odot \text{ yr}^{-1}$  for RXJ1131.

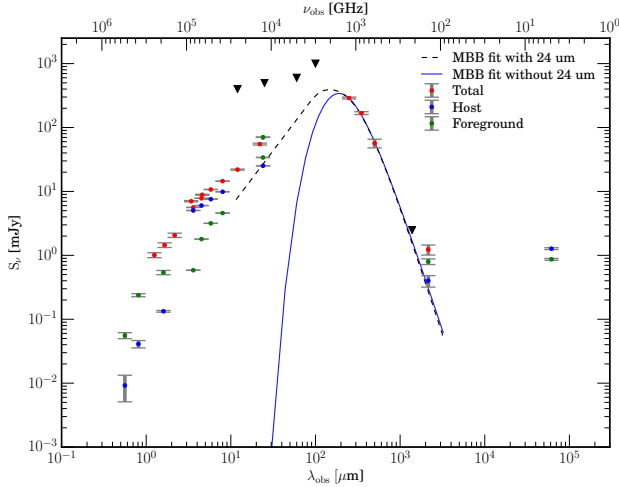


FIG. 10.— SEDs of RXJ1131 at  $z=0.654$  and its lensing galaxy at  $z=0.295$ . The photometry data (colored markers) are not corrected for lensing (see Table 1). Best-fit SED models of the thermal dust emission towards RXJ1131 are obtained assuming a MBB+power-law model. The dashed (solid) line corresponds to a model with (without) MIR constraint at  $24\ \mu\text{m}$ , respectively.

### 5.5.1. Linewidth and Sizes

A FWHM linewidth of  $\Delta v \sim 600 \pm 160\ \text{km s}^{-1}$  found for RXJ1131 by fitting a single Gaussian is considerably larger than those in the C13 sample ( $370\ \text{km s}^{-1}$ ) as well as in local ULIRGs ( $300 \pm 85\ \text{km s}^{-1}$ , with the largest being  $480\ \text{km s}^{-1}$ ; Solomon et al. 1997, hereafter S97). Yet, given the merging nature of these galaxies, a CO linewidth of  $\sim 600\ \text{km s}^{-1}$  may not be surprising. Indeed, a linewidth of  $\Delta v = 750\ \text{km s}^{-1}$  has been observed in a local LIRG (Arp 118; Solomon & Vanden Bout 2005, hereafter SV05). Linewidth of this range ( $\gtrsim 500\ \text{km s}^{-1}$ ) is also commonly observed in high- $z$  starburst galaxies (e.g., Greve et al. 2005, hereafter G05) and high- $z$  quasar host galaxies (e.g., Coppin et al. 2008), which are believed to originate from mergers.

The CO gas in RXJ1131 is  $\sim 6 \pm 3\ \text{kpc}$  in radius (in the source plane), which is more extended than the average of a sample of disk-like U/LIRGs studied by Ueda et al. (2014), but consistent with their range of  $1.1\text{--}9.3\ \text{kpc}$ . Our CO size is also consistent with that of high- $z$  ( $z > 1$ ) galaxies ( $R \sim 4\text{--}20\ \text{kpc}$ ; G05; Daddi et al. 2010; Riechers et al. 2011; Ivison et al. 2011) and local U/LIRGs in the Gao & Solomon (1999) sample ( $R \lesssim 10\ \text{kpc}$ ).

### 5.5.2. Dynamical Mass

Assuming the gas to be virialized, the dynamical mass can be approximated by  $M_{\text{dyn}} \sim \sigma^2 R / G$ , where  $\sigma$  is the velocity dispersion, or the rotational velocity in the case of a rotating disk model (i.e.,  $\sigma = V_{\text{rot}} \sin i$ ). Using a rotational velocity  $V_{\text{rot}} \sin i = 345\ \text{km s}^{-1}$  (see §5.3), we find a dynamical mass of  $M_{\text{dyn}} \sin^2 i (< 6\ \text{kpc}) = 1.7 \times 10^{11}\ M_{\odot}$  enclosed within the CO-emitting region in RXJ1131. If we instead consider the  $\text{CO}(J=2 \rightarrow 1)$  line peak separation ( $\Delta v_{\text{sep}}/2 \sim 200\ \text{km s}^{-1}$ ) as the rotation velocity, we find  $M_{\text{dyn}} \sin^2 i (< 6\ \text{kpc}) = 5.8 \times 10^{10}\ M_{\odot}$ . We derive an inclination angle of  $56.4^\circ$  from the morphological axial ratio of  $a/b \sim 1''.8/3''.25$ , which we estimate from the source-

plane image reconstructed by C06 (Figure 3 in their paper). This corresponds to an inclination-corrected dynamical mass of  $8.3 \times 10^{10}\ M_{\odot} < M_{\text{dyn}} < 25 \times 10^{10}\ M_{\odot}$ . Our estimate should be considered at best an upper limit since the gas in RXJ1131 is unlikely virialized. In the following sections, we use the lower limit  $(8.3 \pm 1.9) \times 10^{10}\ M_{\odot}$  as the dynamical mass as it is derived in a manner similar to what is commonly used in literature (e.g., S97; Downes & Solomon 1998, hereafter DS98; G05).

Using the velocity dispersion ( $\sigma = 30\ \text{km s}^{-1}$ ) obtained by fitting a single Gaussian to the de-lensed line profile of the companion and a half-light radius of  $R_{\text{CO}} = 4.2 \pm 2.8\ \text{kpc}$  from the best-fit lens model, we find a dynamical mass of  $M_{\text{dyn}} = (3.5 \pm 2.3) \times 10^9\ M_{\odot}$  for the companion, assuming an inclination angle of  $i = 30^\circ$ . The uncertainty here only includes that of the CO source size. On the other hand, we find  $M_{\text{dyn}} \sin^2 30^\circ = 5.8 \times 10^8\ M_{\odot}$  if we adopt the better-constrained V-band source size of  $\sim 700\ \text{pc}$  (B08). This dynamical mass is substantially lower than the gas mass, and may be reflecting the dusty nature of the companion.

### 5.5.3. Gas Mass and Gas Ratios

Using the lensing-corrected dust mass, we find a galactic-scale gas-to-dust ratio of  $40 \pm 34$ , which is lower than the statistical average of  $f_{\text{gas-dust}} = 206$  in the C13 sample but well within their broad range of values over the entire sample. Our ratio is also consistent with high- $z$  SMGs (Bothwell et al. 2013) and local ULIRGs (Wilson et al. 2008), but lower in the Milky Way by  $\sim 4\sigma$  (ignoring systematic uncertainties; Li & Draine 2001; Zubko et al. 2004; Draine et al. 2007). We note that the dust mass derived for RXJ1131 is poorly constrained. If we adopt a dust mass from the other SED fit (i.e., without constraints at  $24\ \mu\text{m}$ ), the dust mass would reduce by a factor of  $\sim 2$ .

There are a number of systematic uncertainties associated with the derived gas-to-dust ratio. For instance, the mass opacity coefficient  $\kappa$ , the  $\alpha_{\text{CO}}$  conversion factor, and the brightness temperature ratio  $r_{21}$ . If we instead use the “Galactic”  $\alpha_{\text{CO}}$  value, which may be more appropriate for some ULIRGs (e.g., Papadopoulos et al. 2012) and minor mergers (Narayanan et al. 2012), the gas mass (and thus gas-to-dust ratio) would be  $\sim 6$  times higher. We note that this gas mass is physically feasible based on dynamical mass constraint. On the other hand, we would also obtain a higher gas mass if we assumed sub-thermal excitation between  $\text{CO}(J=2 \rightarrow 1)$  and  $\text{CO}(J=1 \rightarrow 0)$  emission, but we expect this to be a minor effect as CO emission in ULIRGs are typically thermalized up to  $J=3$  or 4. We also note that the gas-to-dust ratio derived for RXJ1131 may be biased low as the gas is likely to be more extended than the dust. Consequently, the overall magnification factor for the CO gas may be lower than the optically thick dust, which dominates the far-IR luminosity, and thus leading to an overestimated dust mass via our adoption of the CO magnification factor.

### 5.5.4. SFE and Depletion Timescales

To first order, the star formation efficiency ( $SFE = L_{\text{FIR}}/M_{\text{gas}}$ ) indicates the star formation rate per unit solar mass of molecular gas available in a galaxy. Using a wavelength range of  $40\text{--}500\ \mu\text{m}$  defined in C13 for the far-IR luminosity, we find an SFE of  $58 \pm 10\ L_{\odot}\ M_{\odot}^{-1}$ , which is on the low end among other U/LIRGs at  $z < 0.6$  (S97; Combes et al. 2011) but consistent with those of low- $z$  spiral galaxies ( $z < 0.1$ ; SV05) and high- $z$  disk-like galaxies (Daddi et al. 2008). Assuming an  $\alpha_{\text{CO}}$  of  $0.8\ M_{\odot}\ (\text{K km pc}^2)^{-1}$ , this would imply that it is converting gas into stars at an efficiency similar to those of “normal” star-forming disk-like galaxies rather than starburst galaxies (Tacconi et al. 2008; Riechers et al. 2011, C13). This is in agreement with its disk-like kinematic signatures.

Results from theoretical simulations have suggested that the disk component of a gas-rich progenitor galaxy can survive merging if it has a low star formation efficiency, which in turn reduces the gravitational torque available to remove the angular momentum of the gas, thereby allowing a higher gas fraction to be retained and redistributed over a large extent in the merged galaxy (Hopkins et al. 2009). In this scenario, it is plausible that RXJ1131 will evolve into a disk galaxy with a small bulge component upon merging given its low SFE and the extended disk.

Assuming the star formation continues at the current rate without gas replenishment, this corresponds to a gas depletion time of  $\tau = 102 \pm 25\ \text{Myr}$ . Since the star formation rate is expected to vary in an interacting system and AGN accretion also consumes some fraction of the gas, the depletion timescale should only be considered as an upper limit.

## 6. DISCUSSION

### 6.1. Fate of RXS J1131–1231

The classical picture for mergers is one where they are responsible for the formation of the local red and passive spheroidal galaxies. With more realistic treatments of star formation and feedback in recent simulations, it has been suggested that it is possible to suppress bulge formation in gas-rich mergers, thereby forming large disks that resemble local spiral galaxies (Springel & Hernquist 2005; Robertson et al. 2006; Hopkins et al. 2009). The extended molecular gas distribution in RXJ1131 together with its low SFE implies that the removal of angular momentum of the gas via gravitational torque is inefficient. Other mechanisms e.g. bar-like structures that are more efficient at removing angular momentum will be required to transform the gas disk of RXJ1131 into a stellar spheroid and evolve into an E/S0 galaxy. Thus, RXJ1131 may retain its disk component and evolve into a disk galaxy upon its final coalescence with the companion.

### 6.2. Velocity Offset and a Recoiling Black Hole

Sluse et al. (2007, hereafter S07) report two sets of AGN lines observed in RXJ1131. The first set of lines is at  $z \sim 0.653$ , including the narrow component of the Balmer lines, the [O III] 4959, 5007 Å lines, and the Mg II 2798 Å absorption line; the second set is at  $z \sim 0.658$ , including the broad component of the Balmer lines and the Mg II 2798 Å

emission line. Using the CO line center redshift as the systemic redshift, the second set of lines is blueshifted by  $\sim 780\ \text{km s}^{-1}$ . This implies that the broad line region (BLR) of the AGN is dynamically offset from the centroid of its host galaxy. We confirm this spatially in the channel maps in Figure 2 and Figure 7, where the line center of the CO gas is not co-spatial with the optical quasar — the point-like images along the lensing arc are offset to the NW of the CO line center emission. On the other hand, we find that the redshift of the [O III] lines tracing the narrow line region (NLR) is fully consistent with the systemic redshift, supporting previous claims that [O III] lines are good proxies to the true systemic redshift (e.g., Vrtilek 1985; Nelson 2000).

One explanation for the offset may arise from the fact that BLRs are gravitationally bound to the central AGN, whereas this condition is not necessary for NLRs. From an SDSS sample of  $>3800$  quasars, Richards et al. (2002) find a median of  $97\ \text{km s}^{-1}$  and a dispersion of  $269\ \text{km s}^{-1}$  in the distribution of the offset between [Mg II] and [O III] lines, suggesting that large offsets are uncommon. Nevertheless, offsets as large as  $\sim 500\ \text{km s}^{-1}$  have been observed in some cases.

Alternatively, large velocity offsets between emission lines of the BLR and the NLR may arise in a recoiling black hole (BH), where its BLR is moving at high velocity relative to the bulk of its host galaxy (Madau & Quataert 2004; Bonning et al. 2007; Loeb 2007). A recoiling black hole is expected when a pair of uneven mass BH coalesce, during which their orbital energy is being released as gravitational wave and a non-zero net angular momentum is being carried away. Depending on their initial conditions, numerical relativity simulations have shown that the recoil velocity can reach up to  $\sim 4000\ \text{km s}^{-1}$  for spinning BHs (e.g., Campanelli et al. 2007). Several sources have been proposed as recoiling BH candidates, such as CID-42 at  $z = 0.359$  (Civano et al. 2010) and SDSS 0956+5127 at  $z \sim 0.714$  (Steinhardt et al. 2012). One notable system is SDSSJ0927+2943 at  $z \sim 0.713$ , where a set of redshifted narrow lines and a second set of blueshifted broad AGN lines have been observed (Komossa et al. 2008), similar to the case for RXJ1131. However, this scenario is refuted recently by Decarli et al. (2014), who confirm that the BLR lines in SDSSJ0927+2943 are consistent with the CO systemic redshift. This is in contrast with RXJ1131, where our CO observations confirm the blueshifted BLR. Since this model requires a merged BH, it would imply that RXJ1131 might have been in a previous merger, which would also explain the highly spinning BH in RX1131 ( $a \sim 0.9$ ; Reis et al. 2014).

### 6.3. The $M_{\text{BH}}\text{--}M_{\text{bulge}}$ Relation

Based on the black hole mass of  $M_{\text{BH}} \sim 8 \times 10^7\ M_{\odot}$  (Sluse et al. 2012), and adopting the stellar mass of  $M^* = 2.95^{+1.32}_{-0.86} \times 10^{10}\ M_{\odot}$  as an upper limit to the bulge mass, we find a  $M_{\text{BH}}/M_{\text{bulge}}$  ratio of 0.19%–0.38%. This is consistent with other intermediate- $z$  radio-loud AGNs (McLure et al. 2006) but lies above the local  $M_{\text{BH}}\text{--}M_{\text{bulge}}$  relation (Häring & Rix 2004). The elevated  $M_{\text{BH}}/M_{\text{bulge}}$



ratio of RXJ1131 compared to local AGNs is consistent with the emerging picture that quasars grow faster than their host galaxies at higher redshifts.

## 7. SUMMARY AND CONCLUSIONS

We present PdBI CO( $J=2 \rightarrow 1$ ) and CARMA CO( $J=3 \rightarrow 2$ ) observations towards the quadruply-imaged quasar RXJ1131 at  $z_{\text{CO}} \sim 0.654$ , making this the first resolved CO study at intermediate redshift. Using the CO line intensities, we find a brightness temperature ratio of  $r_{32} = 0.66 \pm 0.41$  between the CO( $J=2 \rightarrow 1$ ) and CO( $J=3 \rightarrow 2$ ) lines. Taking into account the large phase errors associated with the CO( $J=3 \rightarrow 2$ ) measurement, this is consistent with thermalized excitation. We also detect marginally resolved 2 mm continuum underlying the CO( $J=2 \rightarrow 1$ ) line in the PdBI data and resolved radio continuum emission at 5 GHz in the archival VLA data in both the foreground lensing galaxy and RXJ1131. Using positional priors from an astrometric-corrected *HST* image, we de-blend broadband photometry spanning the rest-frame UV to radio wavelengths that we have compiled from public catalogues and previous optical studies, as well as from those we have extracted using aperture photometry.

Based on our lens modeling analysis of different CO( $J=2 \rightarrow 1$ ) velocity channels, we find a secondary CO-emitting source near RXJ1131 whose coordinates are consistent with those of an optically faint companion reported in previous optical studies (C06; B08). The magnification factor inferred from our best-fit models is found to vary from  $\mu_L \sim 3$  to  $\sim 8$  across channels. This is indicative of an extended molecular gas distribution in the host galaxy of RXJ1131 and thus different kinematic components of the gas are magnified inhomogeneously. Upon correcting for lensing magnification and subtracting a contribution from the companion, we find an intrinsically symmetric double-horned CO( $J=2 \rightarrow 1$ ) line profile for RXJ1131. This together with a symmetric velocity gradient reconstructed in the source plane argues for a rotating disk morphology for RXJ1131, in good agreement with previous findings (C06). Assuming thermalized excitation between CO( $J=1 \rightarrow 0$ ) and CO( $J=2 \rightarrow 1$ ) and  $\alpha_{\text{CO}} = 0.8 M_{\odot} (\text{K km pc}^2)^{-1}$ , we find a lensing-corrected gas mass of  $M_{\text{gas}} = (1.38 \pm 0.33) \times 10^{10} M_{\odot}$  for RXJ1131 and  $(1.92 \pm 0.09) \times 10^9 M_{\odot}$  for the companion. This corresponds to a gas mass ratio of  $\sim 7:1$ . Using the source-plane CO( $J=2 \rightarrow 1$ ) size of  $R \sim 6 \text{ kpc}$  for RXJ1131, we find a dynamical mass of  $M_{\text{dyn}} \sim 8 \times 10^{10} M_{\odot}$ , and thus a gas mass fraction of  $\sim 0.19$ . This gas fraction is consistent with the trend of decreasing molecular gas content since  $z \sim 1$  (e.g., Lagos et al. 2011; Combes et al. 2013) which has been suggested as the cause for the decline in SFR towards  $z \sim 0$  (Carilli & Walter 2013, and references therein). Due to the lack of stringent constraints on the individual galaxy mass of RXJ1131 and of the companion, we classify the system as a “wet” minor merger on the basis of their gas mass ratio.

Fitting dust SED models to the IR-to-mm photometry, we derive lensing-corrected  $M_{\text{dust}} \sim 4 \times 10^8 M_{\odot}$ ,  $L_{\text{IR}}$

$\sim 1.5 \times 10^{12} L_{\odot}$ , and a far-IR luminosity that corresponds to a  $\text{SFR}_{\text{FIR}} \sim 120 M_{\odot} \text{ yr}^{-1}$ . These physical properties suggest that the merger system is dusty in nature with active starburst activity. We also derive a stellar mass of  $M^* \sim 3 \times 10^{10} M_{\odot}$  by fitting SED models to the rest-frame UV-to-mm photometry, which have been corrected for their respective magnification factors before performing the fit, in order to take into account the effect of differential lensing. The source-plane distribution of the gas and stellar populations of different ages indicates that the CO gas is of similar spatial extent as the old and long-lasting stellar populations, whereas recent star formation regions appear to be embedded within the inner few kpc of the molecular gas reservoir. The compact starburst in RXJ1131 is likely a consequence of gas accumulation driven by interactions with the companion. While properties such as CO linewidths, CO size, SFR, and gas mass found in RXJ1131 resemble those of local ULIRGs and high- $z$  starburst galaxies, its SFE is comparable to those of nearby and high- $z$  disk-like galaxies rather than starburst systems. Recent theoretical simulations have illustrated that the disk component of a gas-rich progenitor galaxy with low SFE can be retained upon merging since the efficiency at removing angular momentum of the gas via gravitational torques provided by stellar components is reduced in such a system. As such, the extended molecular gas disk of RXJ1131 together with its low SFE may be indications that the nuclear starburst in RXJ1131 could form a larger stellar bulge in the merger remnant upon coalescing, and yet, the inefficient removal of gas angular momentum renders it unlikely to evolve into an E/S0 galaxy.

Using the CO redshift as the systemic redshift for the host galaxy of RXJ1131, we find that the optical BLR lines reported in previous studies are blueshifted by  $\sim 780 \text{ km s}^{-1}$ . This implies that the AGN is offset from the dynamical center of its host galaxy. One explanation could be that the BLRs are gravitationally bound to the central AGN, whereas this condition is not necessary for NLRs. Since such an offset is typically  $\sim 100 \pm 270 \text{ km s}^{-1}$ , we thus raise an alternative explanation of a recoiling black hole in RXJ1131, which would also explain the highly spinning black hole.

Adopting the stellar mass as an upper limit to the bulge mass of RXJ1131, we find a  $M_{\text{BH}}/M_{\text{bulge}} \gtrsim 0.27\%$ , providing a direct constraint on the empirical  $M_{\text{BH}}-M_{\text{bulge}}$  relation at  $z \sim 0.65$ . The elevated  $M_{\text{BH}}/M_{\text{bulge}}$  ratio compared to the local relation suggests that the black hole in RXJ1131 grows faster or earlier than its host galaxy than the local counterparts. This is consistent with existing studies of the evolution in the co-eval growth between SMBHs and their host galaxies.

This work demonstrates that, with the aid of gravitational lensing and dynamical lens modeling of resolved spectral line observations, it is possible to study the gas kinematics and dynamics in high- $z$  quasar host galaxies despite strong quasar emission. The first use of such technique is presented by Riechers et al. (2008), who reconstruct a source-plane velocity gradient and constrain the gas dynamics in a  $z > 4$  quasar PSS J2322+1944, which

is also the only other similar system whose host galaxy is lensed into an Einstein ring configuration.

This work is based on observations carried out under project number S14BX with the IRAM NOEMA Interferometer. IRAM is supported by INSU/CNRS (France), MPG (Germany) and IGN (Spain). Support for CARMA construction was derived from the Gordon and Betty Moore Foundation, the Kenneth T. and Eileen L. Norris Foundation, the James S. McDonnell Foundation, the Associates of the California Institute of Technology, the University of Chicago, the states of Illinois, California, and Maryland, and the National Science Foundation. Ongoing CARMA development and operations are supported by the National Science Foundation under a cooperative agreement and by the CARMA consortium universities. The National Radio Astronomy Observatory is a facility of the National Science Foundation operated under cooperative agreement by Associated Universities, Inc. This research made use of data obtained with *Herschel*, an ESA space observatory with science instruments provided by European-led Principal Investigator consortia and with important participation from NASA. This research has made use of NASA's Astrophysics Data System Bibliographic Services. This work is based in part on observations made with the *Spitzer Space Telescope*, which is

operated by the Jet Propulsion Laboratory, California Institute of Technology under a contract with NASA. This publication made use of data products from the Wide-field Infrared Survey Explorer, which is a joint project of the University of California, Los Angeles, and the Jet Propulsion Laboratory/California Institute of Technology, funded by the National Aeronautics and Space Administration. This publication made use of data products from the Two Micron All Sky Survey, which is a joint project of the University of Massachusetts and the Infrared Processing and Analysis Center/California Institute of Technology, funded by the National Aeronautics and Space Administration and the National Science Foundation. This research made use of the NASA/IPAC Extragalactic Database (NED) which is operated by the Jet Propulsion Laboratory, California Institute of Technology, under contract with the National Aeronautics and Space Administration. This research made use of Astropy, a community-developed core Python package for Astronomy (Astropy Collaboration et al. 2013). This research made use of APLpy, an open-source plotting package for Python hosted at <http://aplpy.github.com>.

Facilities: IRAM PdBI, CARMA, VLA, *Herschel*(SPIRE), WISE, IRAS, 2MASS, Spitzer(IRAC, MIPS), HST(ACS, NICMOS)

Alexander, D. M., Brandt, W. N., Smail, I., et al. 2008, *AJ*, **135**, 1968  
 Astropy Collaboration, Robitaille, T. P., Tollerud, E. J., et al. 2013, *A&A*, **558**, A33  
 Bonning, E. W., Shields, G. A., & Salvander, S. 2007, *ApJ*, **666**, L13  
 Borys, C., Smail, I., Chapman, S. C., et al. 2005, *ApJ*, **635**, 853  
 Bothwell, M. S., Smail, I., Chapman, S. C., et al. 2013, *MNRAS*, **429**, 3047  
 Brewer, B. J., & Lewis, G. F. 2008, *MNRAS*, **390**, 39  
 Bruzual, G., & Charlot, S. 2003, *MNRAS*, **344**, 1000  
 Bussmann, R. S., Leung, T. K. D., & Conley, A. 2015a  
 Bussmann, R. S., Riechers, D., Fialkov, A., et al. 2015b, *ApJ*, **812**, 43  
 Campanelli, M., Lousto, C. O., Zlochower, Y., & Merritt, D. 2007, *Physical Review Letters*, **98**, 231102  
 Carilli, C. L., & Walter, F. 2013, *ARA&A*, **51**, 105  
 Civano, F., Elvis, M., Lanzuisi, G., et al. 2010, *ApJ*, **717**, 209  
 Claeskens, J.-F., Sluse, D., Riaud, P., & Surdej, J. 2006, *A&A*, **451**, 865  
 Combes, F., García-Burillo, S., Braine, J., et al. 2011, *A&A*, **528**, A124  
 —. 2013, *A&A*, **550**, A41  
 Coppin, K. E. K., Swinbank, A. M., Neri, R., et al. 2008, *MNRAS*, **389**, 45  
 Courteau, S. 1997, *AJ*, **114**, 2402  
 Courteau, S., & Rix, H.-W. 1997, in Bulletin of the American Astronomical Society, Vol. 29, American Astronomical Society Meeting Abstracts, 1332  
 da Cunha, E., Charlot, S., & Elbaz, D. 2008, *MNRAS*, **388**, 1595  
 da Cunha, E., Walter, F., Smail, I. R., et al. 2015, *ApJ*, **806**, 110  
 Daddi, E., Dannerbauer, H., Elbaz, D., et al. 2008, *ApJ*, **673**, L21  
 Daddi, E., Bournaud, F., Walter, F., et al. 2010, *ApJ*, **713**, 686  
 Decarli, R., Dotti, M., Mazzucchelli, C., Montuori, C., & Volonteri, M. 2014, *MNRAS*, **445**, 1558

Di Matteo, T., Springel, V., & Hernquist, L. 2005, *Nature*, **433**, 604  
 Dowell, C. D., Conley, A., Glenn, J., et al. 2014, *ApJ*, **780**, 75  
 Downes, D., & Solomon, P. M. 1998, *ApJ*, **507**, 615  
 Draine, B. T., Dale, D. A., Bendo, G., et al. 2007, *ApJ*, **663**, 866  
 Dunne, L., Eales, S. A., & Edmunds, M. G. 2003, *MNRAS*, **341**, 589  
 Erb, D. K., Steidel, C. C., Shapley, A. E., et al. 2006, *ApJ*, **646**, 107  
 Fazio, G. G., Hora, J. L., Allen, L. E., et al. 2004, *ApJS*, **154**, 10  
 Gao, Y., & Solomon, P. M. 1999, *ApJ*, **512**, L99  
 Greve, T. R., Bertoldi, F., Smail, I., et al. 2005, *MNRAS*, **359**, 1165  
 Häring, N., & Rix, H.-W. 2004, *ApJ*, **604**, L89  
 Hinshaw, G., Larson, D., Komatsu, E., et al. 2013, *ApJS*, **208**, 19  
 Hopkins, A. M., & Beacom, J. F. 2006, *ApJ*, **651**, 142  
 Hopkins, P. F., Cox, T. J., Younger, J. D., & Hernquist, L. 2009, *ApJ*, **691**, 1168  
 Ivison, R. J., Papadopoulos, P. P., Smail, I., et al. 2011, *MNRAS*, **412**, 1913  
 Kennicutt, Jr., R. C. 1998, *ARA&A*, **36**, 189  
 Komossa, S., Zhou, H., & Lu, H. 2008, *ApJ*, **678**, L81  
 Lagos, C. D. P., Baugh, C. M., Lacey, C. G., et al. 2011, *MNRAS*, **418**, 1649  
 Li, A., & Draine, B. T. 2001, *ApJ*, **554**, 778  
 Loeb, A. 2007, *Physical Review Letters*, **99**, 041103  
 Madau, P., & Dickinson, M. 2014, *ARA&A*, **52**, 415  
 Madau, P., & Quataert, E. 2004, *ApJ*, **606**, L17  
 Magorrian, J., Tremaine, S., Richstone, D., et al. 1998, *AJ*, **115**, 2285  
 McLure, R. J., Jarvis, M. J., Targett, T. A., Dunlop, J. S., & Best, P. N. 2006, *MNRAS*, **368**, 1395  
 Miller, S. H., Bundy, K., Sullivan, M., Ellis, R. S., & Treu, T. 2011, *ApJ*, **741**, 115  
 Narayanan, D., Krumholz, M. R., Ostriker, E. C., & Hernquist, L. 2012, *MNRAS*, **421**, 3127  
 Nelson, C. H. 2000, *ApJ*, **544**, L91  
 Neugebauer, G., Habing, H. J., van Duinen, R., et al. 1984, *ApJ*, **278**, L1

- Ott, S. 2010, in *Astronomical Society of the Pacific Conference Series*, Vol. 434, *Astronomical Data Analysis Software and Systems XIX*, ed. Y. Mizumoto, K.-I. Morita, & M. Ohishi, 139
- Papadopoulos, P. P., van der Werf, P., Xilouris, E., Isaak, K. G., & Gao, Y. 2012, *ApJ*, **751**, 10
- Peng, C. Y., Impey, C. D., Rix, H.-W., et al. 2006, *ApJ*, **649**, 616
- Pooley, D., Blackburne, J. A., Rappaport, S., & Schechter, P. L. 2007, *ApJ*, **661**, 19
- Puech, M., Flores, H., Hammer, F., et al. 2008, *A&A*, **484**, 173
- Reis, R. C., Reynolds, M. T., Miller, J. M., & Walton, D. J. 2014, *Nature*, **507**, 207
- Richards, G. T., Vanden Berk, D. E., Reichard, T. A., et al. 2002, *AJ*, **124**, 1
- Riechers, D. A., Hodge, J., Walter, F., Carilli, C. L., & Bertoldi, F. 2011, *ApJ*, **739**, L31
- Riechers, D. A., Walter, F., Brewer, B. J., et al. 2008, *ApJ*, **686**, 851
- Riechers, D. A., Bradford, C. M., Clements, D. L., et al. 2013, *Nature*, **496**, 329
- Rieke, G. H., Young, E. T., Engelbracht, C. W., et al. 2004, *ApJS*, **154**, 25
- Robertson, B., Bullock, J. S., Cox, T. J., et al. 2006, *ApJ*, **645**, 986
- Sajina, A., Yan, L., Fadda, D., Dasyra, K., & Huynh, M. 2012, *ApJ*, **757**, 13
- Salpeter, E. E. 1955, *ApJ*, **121**, 161
- Skrutskie, M. F., Cutri, R. M., Stiening, R., et al. 2006, *AJ*, **131**, 1163
- Sluse, D., Claeskens, J.-F., Hutsemékers, D., & Surdej, J. 2007, *A&A*, **468**, 885
- Sluse, D., Hutsemékers, D., Courbin, F., Meylan, G., & Wambsganss, J. 2012, *A&A*, **544**, A62
- Sluse, D., Surdej, J., Claeskens, J.-F., et al. 2003, *A&A*, **406**, L43
- Solomon, P. M., Downes, D., Radford, S. J. E., & Barrett, J. W. 1997, *ApJ*, **478**, 144
- Solomon, P. M., & Vanden Bout, P. A. 2005, *ARA&A*, **43**, 677
- Springel, V., & Hernquist, L. 2005, *ApJ*, **622**, L9
- Steinhardt, C. L., Schramm, M., Silverman, J. D., et al. 2012, *ApJ*, **759**, 24
- Stern, D., Eisenhardt, P., Gorjian, V., et al. 2005, *ApJ*, **631**, 163
- Tacconi, L. J., Genzel, R., Smail, I., et al. 2008, *ApJ*, **680**, 246
- Ueda, J., Iono, D., Yun, M. S., et al. 2014, *ApJS*, **214**, 1
- Vrtilek, J. M. 1985, *ApJ*, **294**, 121
- Walter, F., Carilli, C., Bertoldi, F., et al. 2004, *ApJ*, **615**, L17
- Walter, F., Decarli, R., Sargent, M., et al. 2014, *ApJ*, **782**, 79
- Wilson, C. D., Petitpas, G. R., Iono, D., et al. 2008, *ApJS*, **178**, 189
- Wright, E. L., Eisenhardt, P. R. M., Mainzer, A. K., et al. 2010, *AJ*, **140**, 1868
- Zubko, V., Dwek, E., & Arendt, R. G. 2004, *ApJS*, **152**, 211